

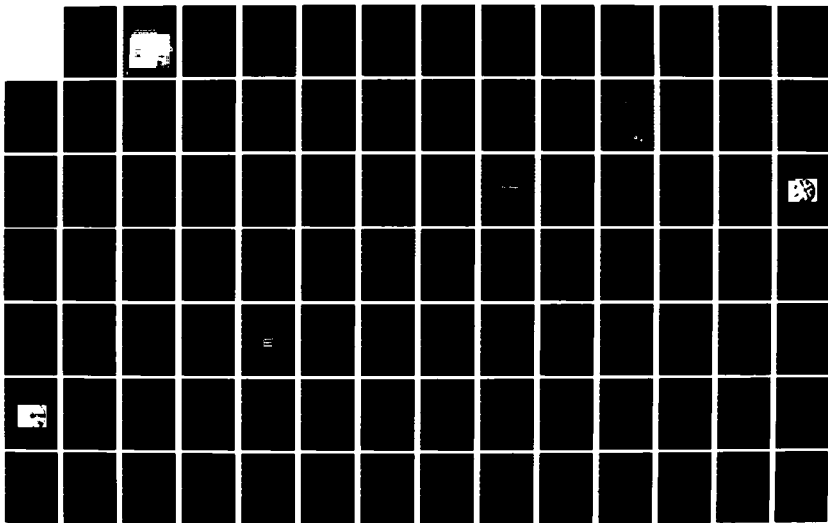
AD-A124 465

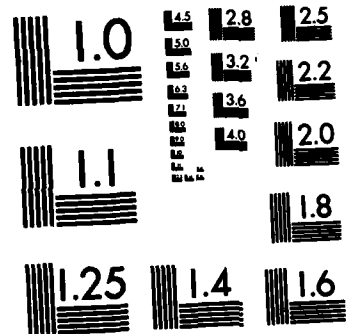
LASER ANNEALING OF ION IMPLANTED SILICON(U) ILLINOIS  
UNIV AT URBANA COORDINATED SCIENCE LAB A BHATTACHARYYA  
RUG 81 R-912 N00014-79-C-0424

1/2

UNCLASSIFIED

.F/G 20/12 NL

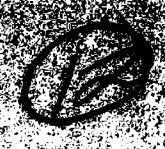




MICROCOPY RESOLUTION TEST CHART  
NATIONAL BUREAU OF STANDARDS-1963-A

REPORT 18-012 AUGUST 1981

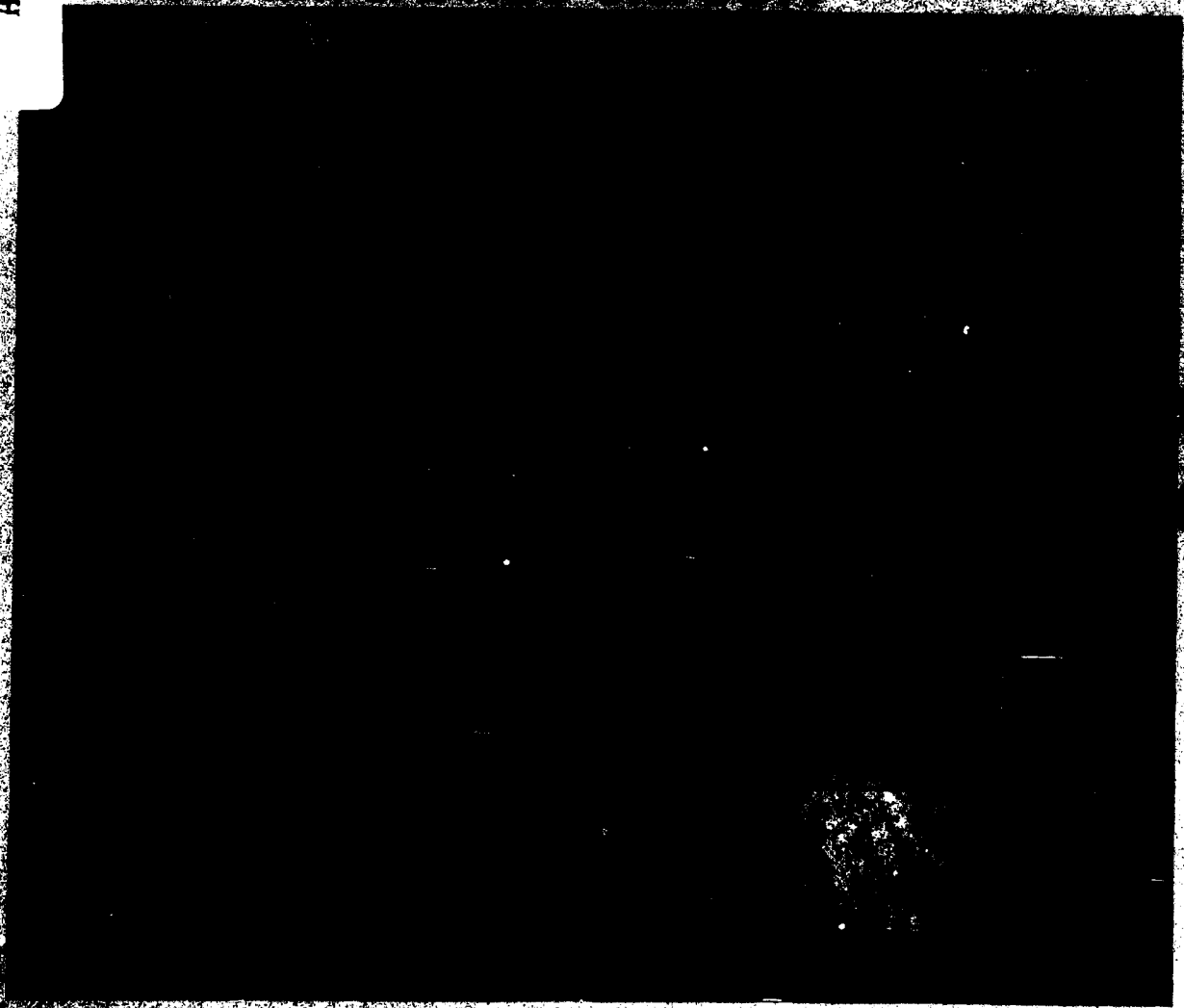
UILL-ENG 81-2243



**COORDINATED SCIENCE LABORATORY**

ADA 124465

**LASER ANNEALING OF  
ION IMPLANTED SILICON**



**UNIVERSITY OF ILLINOIS AT URBANA-CHAMPAIGN**

**83 02 016 038**

UNCLASSIFIED

SECURITY CLASSIFICATION OF THIS PAGE (When Data Entered)

REPORT DOCUMENTATION PAGE		READ INSTRUCTIONS BEFORE COMPLETING FORM
1. REPORT NUMBER	2. GOVT ACCESSION NO.	3. RECIPIENT'S CATALOG NUMBER
	JD-A124 465	
4. TITLE (and Subtitle)		5. TYPE OF REPORT & PERIOD COVERED
LASER ANNEALING OF ION IMPLANTED SILICON		Technical Report
		6. PERFORMING ORG. REPORT NUMBER
		R-912 UILU-ENG 81-2243
7. AUTHOR(s)		8. CONTRACT OR GRANT NUMBER(s)
ANJAN BHATTACHARYYA		N00014-79-C-0424 DAAG 29-80-C-0011
9. PERFORMING ORGANIZATION NAME AND ADDRESS		10. PROGRAM ELEMENT, PROJECT, TASK AREA & WORK UNIT NUMBERS
Coordinated Science Laboratory, 1101 W. Springfield University of Illinois, Urbana, IL 61801		
11. CONTROLLING OFFICE NAME AND ADDRESS		12. REPORT DATE
		August, 1981
		13. NUMBER OF PAGES
		90
14. MONITORING AGENCY NAME & ADDRESS (if different from Controlling Office)		15. SECURITY CLASS. (of this report)
		UNCLASSIFIED
		15a. DECLASSIFICATION/DOWNGRADING SCHEDULE
16. DISTRIBUTION STATEMENT (of this Report)		
Approved for public release; distribution unlimited		
17. DISTRIBUTION STATEMENT (of the abstract entered in Block 20, if different from Report)		
18. SUPPLEMENTARY NOTES		
19. KEY WORDS (Continue on reverse side if necessary and identify by block number)		
Laser Annealing Ion Implanted Silicon		
20. ABSTRACT (Continue on reverse side if necessary and identify by block number)		
<p>We present here a detailed theoretical and experimental investigation of the dynamics of surface melting and regrowth and electrical activation of Si<sup>+</sup> and BF<sub>2</sub><sup>-</sup> ion implanted amorphized silicon annealed with a Q-switched Nd:glass laser (<math>\lambda = 1.06 \mu\text{m}</math>). In the theoretical calculations we have used the technique of finite difference equations to solve the one-dimensional heat conduction equations for the solid and liquid phases. We have taken into account the temperature dependence of all the parameters involved to give us</p>		

DD FORM 1473  
1 JAN 73

UNCLASSIFIED

SECURITY CLASSIFICATION OF THIS PAGE (When Data Entered)

20. a realistic model. The melting model is supported by time resolved reflectivity measurements using a He-Ne and an Ar laser. We use SEM to investigate the electron channeling pattern to study the quality of crystalline regrowth. For  $\text{BF}_2^+$  implanted silicon, the boron and fluorine atomic profiles are measured by secondary ion mass spectrometry (SIMS) on as-implanted samples as well as laser annealed samples. The impurity redistribution is explained on the basis of the melting model. Differential resistivity and Hall effect measurements in conjunction with successive layer removal are used to obtain the electrical carrier distributions as a function of the laser fluence. For good quality crystalline regrowth and full electrical activation, the laser fluence should lie between the melting threshold and the damage threshold. Therefore, a reliable model is useful in designing experiments of laser annealing.

Pulsed  $\text{CO}_2$  lasers ( $\lambda = 10.6 \mu\text{m}$ ) have the distinct advantage of having considerably larger spot-size than a Nd:glass, YAG or Ruby laser, and are therefore very promising for laser annealing of large Si wafers commonly used in industrial production. At  $10.6 \mu\text{m}$ , the absorption coefficient of amorphous silicon is much smaller than that of crystalline silicon having large donor concentration. Hence, for annealing with a  $\text{CO}_2$  laser it is advantageous to implant the sample with a moderately high ion dose without driving the sample amorphous.

We present a calculation of the temperature rise and investigate the "thermal runaway" phenomenon during pulsed  $\text{CO}_2$  laser annealing of silicon. The calculations are based on the thermal melting model, taking into account the temperature dependence of all pertinent material parameters, including the absorption coefficient. In calculating the temperature variation of free carrier absorption in n-Si, we have taken into account acoustic deformation potential scattering, optical deformation potential scattering, and ionized impurity scattering. The deformation potentials are adjusted to fit the experimentally observed values at  $300^\circ\text{K}$ .

LASER ANNEALING OF ION IMPLANTED SILICON

by

Anjan Bhattacharyya

This work was supported by the Joint Services Electronics Program (U. S. Army, U. S. Navy and U. S. Air Force) under Contract N00014-79-C-0424 and by the Army Research Office under Contract DAAG 29-80-C-0011.

Reproduction in whole or in part is permitted for any purpose of the United States Government.

Accession For	
NTIS GRA&I	<input checked="" type="checkbox"/>
DTIC TAB	<input type="checkbox"/>
Unannounced	<input type="checkbox"/>
Justification	
Distribution/	
Availability Codes	
Avail and/or	
Dist	Special
A	



Approved for public release. Distribution unlimited.

LASER ANNEALING OF ION IMPLANTED SILICON

BY

ANJAN BHATTACHARYYA

B.A., University of Cambridge, 1976

M.S., University of Illinois, 1979

THESIS

Submitted in partial fulfillment of the requirements  
for the degree of Doctor of Philosophy in Electrical Engineering  
in the Graduate College of the  
University of Illinois at Urbana-Champaign, 1981

Thesis Advisor: B. G. Streetman

Urbana, Illinois

## LASER ANNEALING OF ION IMPLANTED SILICON

Anjan Bhattacharyya, Ph.D.  
Coordinated Science Laboratory and  
Department of Electrical Engineering  
University of Illinois at Urbana-Champaign, 1981

We present here a detailed theoretical and experimental investigation of the dynamics of surface melting and regrowth and electrical activation of  $\text{Si}^+$  and  $\text{BF}_2^+$  ion implanted amorphized silicon annealed with a Q-switched Nd:glass laser ( $\lambda = 1.06 \mu\text{m}$ ). In the theoretical calculations we have used the technique of finite difference equations to solve the one-dimensional heat conduction equations for the solid and liquid phases. We have taken into account the temperature dependence of all the parameters involved to give us a realistic model. The melting model is supported by time resolved reflectivity measurements using a He-Ne and an Ar laser. We use SEM to investigate the electron channelling pattern to study the quality of crystalline regrowth. For  $\text{BF}_2^+$  implanted silicon, the boron and fluorine atomic profiles are measured by secondary ion mass spectrometry (SIMS) on as-implanted samples as well as laser annealed samples. The impurity redistribution is explained on the basis of the melting model. Differential resistivity and Hall effect measurements in conjunction with successive layer removal are used to obtain the electrical carrier distributions as a function of the laser fluence. For good quality crystalline regrowth and full electrical activation, the laser fluence should lie between the melting threshold and the damage threshold. Therefore, a reliable model is useful in designing experiments of laser annealing.

Pulsed  $\text{CO}_2$  lasers ( $\lambda = 10.6 \mu\text{m}$ ) have the distinct advantage of having

considerably larger spot-size than a Nd:glass, YAG or Ruby Laser, and are therefore very promising for laser annealing of large Si wafers commonly used in industrial production. At 10.6  $\mu\text{m}$ , the absorption coefficient of amorphous silicon is much smaller than that of crystalline silicon having large donor concentration. Hence, for annealing with a  $\text{CO}_2$  laser it is advantageous to implant the sample with a moderately high ion dose without driving the sample amorphous.

We present a calculation of the temperature rise and investigate the "thermal runaway" phenomenon during pulsed  $\text{CO}_2$  laser annealing of silicon. The calculations are based on the thermal melting model, taking into account the temperature dependence of all pertinent material parameters, including the absorption coefficient. In calculating the temperature variation of free carrier absorption in n-Si, we have taken into account acoustic deformation potential scattering, optical deformation potential scattering, and ionized impurity scattering. The deformation potentials are adjusted to fit the experimentally observed values at 300°K.

## ACKNOWLEDGMENTS

The author wishes to express his gratefulness to Professor B. G. Streetman for his guidance and support.

The author thanks Professor Karl Hess for his invaluable direction during the development of the melting model.

He is indebted to Dr. H. Shichijo for help with the computer programming; L. A. Reinisch of the Physics Department for providing us with the laser facilities; J. E. Baker and Dr. P. Williams for SIMS measurements, J. Woodhouse for teaching how to use the SEM.

He sincerely appreciates the assistance and friendship of his colleagues, K. Soda, M. Keever, V. Iyer, P. Martin, S. S. Chan, Sanjay Banerjee, R. DeJule and J. D. Oberstar.

The author thanks E. M. Kesler, M. Ray and Susan Brennecke for careful typing of this manuscript.

## TABLE OF CONTENTS

CHAPTER	Page
1. INTRODUCTION.....	1
1.1 Melting Model.....	3
1.2 Ion Implantation.....	10
2. LASER ANNEALING OF $\text{Si}^+$ IMPLANTED AMORPHIZED SILICON.....	15
2.1 Theoretical Results.....	15
2.2 Sample Preparation.....	21
2.3 Time-Resolved Reflectivity Measurements.....	23
2.4 Experimental Results and Comparisons with the Melting Model.....	25
2.5 Electron Channeling Pattern Using a Scanning Electron Microscope.....	29
3. LASER ANNEALING OF $\text{BF}_2^+$ IMPLANTED AMORPHIZED SILICON.....	32
3.1 Theoretical Results.....	33
3.2 Sample Preparation.....	40
3.3 Time-Resolved Reflectivity Measurements.....	40
3.4 Atomic Profiling.....	42
3.5 Electrical Profiling.....	47
3.5.1 Hall System.....	47
3.5.2 Sample Preparation.....	49
3.5.3 Data Analysis.....	51
3.5.4 Experimental Results.....	52
3.6 Electron Channeling Pattern using a Scanning Electron Microscope.....	56
4. DYNAMICS OF PULSED $\text{CO}_2$ LASER ANNEALING OF SILICON.....	61
REFERENCES.....	79
APPENDIX A Computer program for calculation of the dynamics of surface melting during pulsed laser annealing of an infinite ion-implanted amorphized semi- conductor.....	82
VITA.....	90

## I. INTRODUCTION

The technique of ion implantation in semiconductors for device fabrication is accompanied by radiation damage. Conventionally, thermal annealing has been employed to restore the lattice to crystalline order and to provide for electrical activation of the dopant atoms. It has been shown recently [1] that an intense laser light of short pulse duration has several advantages over thermal annealing of ion-implanted amorphized thin layers in Si. We present below a detailed account of a thermal melting model to explain the physical mechanism behind pulsed laser annealing. The model is experimentally supported by time-dependent optical reflectivity measurements. Similar calculations have been done with slightly different assumptions for ion-implanted silicon [2] and crystalline silicon [3]. The present calculations are compared with results of time-resolved reflectivity measurements for pulsed annealing at 1.06  $\mu\text{m}$  of an amorphous layer produced by implants of  $\text{Si}^+$  in Si and  $\text{BF}_2^+$  in Si. Comparison of the calculations and the experimental model support the assumption that the Si surface melts during pulsed laser annealing of appropriate power density. The thermal melting model is also supported by atomic impurity profiling using the SIMS technique, described by Wang et al. [4] and analysis of electron-beam induced current using SEM, described by Jastrzebski et al [5].

For good quality crystalline regrowth, the laser fluence should lie between the melting threshold and the damage threshold. It is also important to adjust the laser and the material parameters such that the

melt front propagates through the amorphous-crystalline interface and wets the substrate. Otherwise, polycrystalline growth occurs. Therefore, a predictive model is very useful in choosing appropriate experimental conditions.

For a particular thickness of the amorphous layer, the incident laser energy and the pulse width of the laser beam are used as parameters to determine the duration of the surface melting and the time-evolution of the melt front into the material. The numerical technique used in solving the nonlinear heat conduction equations is the finite difference method. The formalism can be applied to Ge, GaAs, and other materials and also to various lasers such as ruby, CO<sub>2</sub>, etc. The material parameters and the absorption mechanisms for the different laser wavelengths must be taken into consideration, but the theoretical methods are similar.

We note that in the visible and near infrared region, the absorption coefficient of amorphous silicon [6] is an order of magnitude or more higher than that of crystalline silicon. We take this factor into consideration in determining the threshold energy density of melting of ion-implanted amorphized silicon.

The phenomenon of pulsed laser annealing and the experimental results of time-resolved reflectivity measurements are explained on the basis of a melting model. There have been speculations, by Van Vechten et al. [7] from theoretical considerations and by Lo and Compaan [8] using Raman measurements, about the possible role of a dense electron-hole plasma which might prevent the lattice temperature from rising significantly during pulsed laser annealing of silicon. However, we find good agreement between the rather simple melting model and results of reflectivity experi-

ments, without invoking plasma effects. The present work and time-resolved reflectivity measurements obtained by Nathan et al., [9] suggest that the rise in reflectivity of the Si surface and the resulting recrystallization is caused by thermal melting for typical pulsed laser annealing experiments, and is most likely not a result of the formation of a dense electron-hole plasma which prevents a significant rise in temperature.

### 1.1 Melting Model

We begin with the ion implanted amorphized silicon at room temperature in the solid phase. The laser light is then absorbed in the near surface region of the solid. The power absorbed by the solid can be expressed by a source term which is both spatial and time dependent. The absorbed light energy is then converted into heat, which diffuses into the bulk by thermal conduction. The above process can be explained by considering the heat conduction equation with an appropriate source term.

The temperature at the surface rises and eventually reaches the melting point of silicon. The melt front propagates into the material, reaches a maximum value and then recedes toward the surface, leading to a liquid-phase epitaxial regrowth. When we have both the liquid and solid phases present, we have to solve simultaneously two heat conduction equations for the two phases. The position of the melt front is also calculated at every time step. Finally, we have crystalline silicon in the solid phase at room temperature.

Since the typical laser spot is about 3 mm in diameter and the pulse is uniform, it is appropriate to neglect the radial flow of heat and consider only the one-dimensional flow of heat into the material.

The one-dimensional heat flow is described by the equation

$$C(T) \rho \frac{\partial T}{\partial t} = \frac{\partial}{\partial x} \left[ \kappa(T) \frac{\partial T}{\partial x} \right] + S(x,t) \quad (1.1)$$

where  $\kappa$  is the thermal conductivity,  $C$  is the specific heat capacity, and  $\rho$  is the density of the material. The source term  $S$  is governed by the mechanism of the laser-solid interaction and the time shape of the laser pulse. The laser pulse is assumed to be Gaussian, and so the time-dependent part of the source term is given by

$$S(t) = \frac{1}{\pi^{1/2} \Gamma} \exp - \left( \frac{t-t'}{\Gamma} \right)^2 \quad (1.2)$$

where  $\Gamma$  is the full width duration of the pulse at  $1/e$  intensity and  $t'$  is the time when the pulse reaches its maximum value.

After the front surface has melted, the heat flow into the liquid is described by an equation similar to (1.1) with the appropriate parameters for the liquid phase.

The boundary conditions employed are

(a) as  $x \rightarrow \infty$ ,  $T \rightarrow 300^\circ\text{K}$

(b)  $\frac{\partial T}{\partial x} = 0$  at  $x = 0$ . The boundary condition must be appropriately

modified to consider evaporation effects at the highest laser energies.

Since the thermal conductivity and specific heat capacity are both temperature dependent, equation (1.1) is essentially nonlinear. We employ the technique of finite-difference equations to solve equation (1.1) for both the solid and liquid phases, taking into account appropriate time-dependent boundary conditions to find the position of the melt front ( $x_m$ ) as a function of time.

At any time,  $x_m$  is obtained from solution of the equation

$$\kappa_s \left. \frac{\partial T}{\partial x} \right|_{x_m} = \kappa_L \left. \frac{\partial T}{\partial x} \right|_{x_m} + L \frac{dx_m}{dt} \quad (1.3)$$

where  $\kappa_s$ ,  $\kappa_L$  are the thermal conductivities of the solid and liquid phases and  $L$  is the latent heat of melting. Equation (1.3) was used in the numerical computations to study the time evolution of the melt-front.

We note that we are considering a first-order phase transition involving latent heat with the density  $\rho$  as the order parameter. Hence the density  $\rho$  cannot be considered to be constant during the phase change as was assumed by Schultz and Collins [10].

We have considered the temperature variation of thermal conductivity [11] and specific heat capacity [12] of Si in the solid phase. The variation of  $\kappa_s$  with temperature turns out to be crucial in calculating the temperature rise during laser annealing. The thermal conductivity of liquid Si has the value  $0.322 \text{ W/cm}^\circ\text{K}$  [13]. Surko et al. [3] used a value of  $\kappa_L$  obtained from  $\sigma_L$  using the Wiedemann-Franz law. However, in view of the small proportion of the electronic contribution for the near melting solid, any estimation of the thermal conductivity of molten silicon from the electrical conductivity is not a good approximation. In our work the specific heat capacity  $C_L$  of liquid Si was assumed [12] to have a constant value of  $0.915 \text{ J/g}^\circ\text{K}$ , since its variation with temperature is not significant. In our calculations we have used the values for crystalline silicon when considering the temperature variation of the thermal conductivity and specific heat capacity of the ion-implanted amorphized silicon layer. There are no available data on the values of  $\kappa_s$  and  $C_s$  for amorphous

silicon from 300°K to 1685°K. However, the difference in the thermal properties between crystalline and amorphous silicon is less pronounced at room temperature than at low temperatures, and becomes negligible as the sample temperature rises from 300°K to 1685°K. For liquid silicon, the values of  $\kappa_L$  and  $C_L$  are independent of whether the sample melted from an amorphous or a crystalline phase in the solid state. The density in the solid and liquid phases is 2.329 g/cm<sup>3</sup> and 2.53 g/cm<sup>3</sup>, respectively. To have the calculations and experiment agree reasonably well, the temperature variations of all the parameters must be considered fully. Schultz and Collins [10] assumed the specific heat of silicon to be constant over the whole temperature range. Baeri et al. [14] have considered the variation of the thermal conductivity of silicon in the solid phase, but have assumed the other parameters to be constant.

Before melting, the spatial part of the source term is given by

$$S_s(x) = E(1-R_s) \alpha_s e^{-\alpha_s x} \quad (1.4)$$

where  $E$  is the fluence of the laser pulse in J/cm<sup>2</sup>,  $R_s$  is the reflectivity, and  $\alpha_s$  is the absorption coefficient. Ideally, one has to consider the effect of the crystalline substrate when the thickness of the implanted amorphized layer is less than  $\alpha_s^{-1}$ . We note that our present assumption will give values of calculated temperatures somewhat higher than the experimental situation. At 1.06  $\mu$ m, the value of the absorption coefficient for crystalline silicon at 300°K is about 10/cm and increases considerably as the sample temperature rises during pulsed laser annealing. This temperature dependent absorption coefficient introduces an additional non-linearity and consequently further complications in the calculation. One

can qualitatively appreciate the fact that, as the thickness of the amorphous layer increases, the effect of the crystalline substrate decreases. Finally, when the thickness of the amorphous layer is two to three times higher than  $\alpha_s^{-1}$ , one can possibly neglect the substrate effect without much loss of accuracy.

After melting, the source term has an expression similar to Eq. (1.4), with  $R_L$  as the reflectivity and  $\alpha_L$  the absorption coefficient of liquid silicon.

$$S_L(x) = E(1-R_L) \alpha_L e^{-\alpha_L x} \quad (1.5)$$

For the case of a Nd:glass laser, the values of  $R_s$  and  $R_L$  were taken to be 0.31 and 0.76, respectively [15,16]. This large change in the value of reflectivity during phase transitions was considered throughout the calculations and was monitored experimentally during time-resolved reflectivity measurements. At 1.06  $\mu\text{m}$ , the values of  $\alpha_s$  [15] for a-Si and  $\alpha_L$  [16] for liquid silicon are given by  $6 \times 10^3/\text{cm}$  and  $1.4 \times 10^6/\text{cm}$ , respectively. We note that the value of  $\alpha_L$  is about two orders of magnitude higher than  $\alpha_s$ . Therefore, after the front surface has melted, we neglect the transmission of laser energy through the liquid phase. This is justifiable as the value of  $\alpha_L^{-1}$  is about 70  $\text{\AA}$  and all the laser energy is absorbed by the thin liquid layer.

To estimate the effect of transmission of the incident laser energy from the liquid to the solid phase, one can neglect changes in the reflection coefficient during melting and write for the source terms in the solid (s) and liquid (L):

$$S_s(x) = E_s(1-R_s) \alpha_s e^{-\alpha_s x} \quad (1.6)$$

and

$$S_L(x) = E_L(1-R_s) \alpha_L e^{-\alpha_L x} \quad (1.7)$$

To determine  $E_s$  and  $E_L$  in the spirit of the above approximation, we apply the following boundary conditions:

(a) At the junction of separation of the two phases, the source term should be continuous,

$$\text{at } x = x_m, S_s(x_m) = S_L(x_m) \quad (1.8)$$

(b) The absorbed total energy density  $E$  is distributed between the liquid and solid phases (and does not change during melting),

$$E \approx \int_0^{x_m} S_L(x) dx + \int_{x_m}^{\infty} S_s(x) dx \quad (1.9)$$

From equations (1.6 - 1.9) we obtain:

$$S_s(x) \approx \frac{E(1-R_s) \alpha_s e^{-\alpha_s (x-x_m)}}{1 + \frac{\alpha_s}{\alpha_L} (e^{\alpha_L x_m} - 1)} \quad (1.10)$$

and

$$S_L(x) \approx \frac{E(1-R_s) \alpha_s e^{-\alpha_L (x-x_m)}}{1 + \frac{\alpha_s}{\alpha_L} (e^{\alpha_L x_m} - 1)} \quad (1.11)$$

We point out that using (1.10) and (1.11) would prevent taking into account the important difference between  $R_s$  and  $R_L$ . Equations (1.10) and (1.11) were not included in the actual computations. Since the large difference between  $R_s$  and  $R_L$  is a major concept in the melting model, we have used equations (1.4) and (1.5) in our computations. Bell [2] has

adopted a different approach in considering the transmission of laser energy from the liquid to solid. When the liquid layer exceeds a value of  $300 \text{ \AA}$ , Bell assumes that all of the incident light that is not reflected is absorbed within the first  $500 \text{ \AA}$ -thick meshpoint. For a liquid layer of thickness less than  $300 \text{ \AA}$  the details of transmittance is taken into account. However, as pointed out by Bell, this detailed consideration during initiation of the melted layer does not have a large effect on the results of the computation. Since for a laser fluence of  $2.0 \text{ J/cm}^2$  the melt-front reaches a maximum value of more than  $4000 \text{ \AA}$ , the details of the transmission in the first  $300 \text{ \AA}$  liquid layer should be rather insignificant. As discussed above, since the value of  $\alpha_L$  ( $1.4 \times 10^6 / \text{cm}$ ) is much larger than the value of  $\alpha_s$  ( $6 \times 10^3 / \text{cm}$ ), we are justified in neglecting the transmission of laser energy from liquid to solid after the front surface has melted.

To solve equation (1.1) numerically we divide the sample into equal sections of length  $\Delta x$ . The time step is denoted by  $\Delta t$ . The intervals  $\Delta x$  and  $\Delta t$  are chosen to satisfy the von Neumann stability criterion given by

$$\Delta t < \frac{C_0}{2\kappa} (\Delta x)^2$$

Specifically, we choose  $\Delta x = 250 \text{ \AA}$  and  $\Delta t = 2 \text{ psec}$  for our calculation. The thickness of a sample was chosen to be  $50 \text{ \mu m}$  for numerical computations. If  $n$  and  $m$  denote a particular set of spatial and time coordinates, then a typical expression for the temperature as a solution to equation (1.1) is given by

$$T_n^m = T_n^{m-1} + \left[ \frac{1}{\Delta x} \left( \kappa_{s1} \frac{T_{n+1}^{m-1} - T_n^{m-1}}{\Delta x} - \kappa_{s2} \frac{T_n^{m-1} - T_{n-1}^{m-1}}{\Delta x} \right) + S_s(x_n, t_m) \right] \frac{\Delta t}{\rho_s C_s (T_n^{m-1})} \quad (1.12)$$

where  $\kappa_{s1} = \frac{1}{2} \left[ \kappa_s (T_{n+1}^{m-1}) + \kappa_s (T_n^{m-1}) \right]$ ,

$$\kappa_{s2} = \frac{1}{2} \left[ \kappa_s (T_n^{m-1}) + \kappa_s (T_{n-1}^{m-1}) \right],$$

Similar equations govern the temperature rise in the liquid phase.

## 1.2 Ion Implantation

Ion implantation is now a standard technique of doping semiconductors and has been extensively reviewed in the literature [17-21]. Basically, ion implantation consists of energetic ions entering the substrate and losing energy through collisions with the lattice until they come to rest in the substrate. The distribution of ions in the substrate is a function of the incident ion species and its energy, along with properties of the substrate material. The two major forms of energy loss for the incoming ion are interactions with the electrons of the substrate atoms and collisions with the nuclei. While only approximately true, these two loss mechanisms can be assumed to be independent of one another. Under this assumption we can write

$$\frac{-dE}{dx} = N \left[ S_n(E) + S_e(E) \right] \quad (1.13)$$

where  $E$  is the energy of the ion at a point  $x$  along its path,  $S_n(E)$  is the nuclear stopping power,  $S_e(E)$  is the electronic stopping power, and  $N$  is the average number of target atoms per unit volume.

To a fairly good approximation, the nuclear stopping power can be assumed to be elastic scattering processes, independent of one another. In the context of these assumptions, the collisions can be treated with classical mechanics. When a potential which takes into account the screening of electrons is used, fairly accurate values of the nuclear stopping power can be obtained.

The electronic stopping power is more difficult to compute theoretically. There are basically two different models that have been used to calculate this quantity. The first method approximates the electrons in the target by a free electron gas. In this approximation the ion loses energy by collisions with the electrons and excitation of plasma resonances. For ion velocities less than that of an electron having an energy below the Fermi energy of the gas, Lendhard and Winther [22] have shown that  $S_e(E)$  can be given by

$$S_e(E) = CV = kE^{\frac{1}{2}} \quad (1.14)$$

where the parameter  $k$  is a function of the ion and substrate involved.

The other model, proposed by Firsov [23], is based on the electronic interactions in a two-body collision. The process may be visualized by the two atoms forming a "quasi-molecule" as they approach each other. The atoms will exchange outer electrons as they attempt to form a molecule. These electrons will take on the net momentum of the "quasi-molecule". When the atoms separate again, the incoming ion will have lost energy to the stationary one. While the Firsov model assumes participation of all the electrons, it is more appropriate to assume some screening from the

inner electrons. Electronic stopping power is more important for high energies and light ions, while nuclear stopping is the major force for low energies and heavy ions.

Once  $S_n$  and  $S_e$  are known, they can be substituted into equation 1.13, and the total distance or range ( $R$ ) the ion travels on its winding path in the substrate can be found. Experimentally, we can only observe the distance travelled perpendicular to the surface, the projected range ( $R_p$ ). Also, since the ions suffer collisions in a random fashion, the ions will come to rest in some type of distribution about the projected range. The spread of the distribution is defined by the standard deviation ( $\Delta R$ ), and the spread perpendicular to the surface is described by the projected standard deviation ( $\Delta R_p$ ).

Differential equations for computing  $R_p$  and  $\Delta R_p$  have been derived by Lindhard, Scharff, and Schiott [24]. This theory, henceforth referred to as LSS, describes the basic features of the implanted profile. The implanted profile can usually be approximated by a gaussian function given by

$$N(x) = N_p \exp \frac{-(x - R_p)^2}{2\Delta R_p^2} \quad (1.15)$$

where  $N(x)$  is the concentration of atoms ( $\text{cm}^{-3}$ ) at a point  $x$  and  $N_p$  is the peak concentration. This peak concentration is expressed by

$$N_p = \frac{0.4}{\Delta R_p} N_D \quad (1.16)$$

where  $N_D$  is the fluence or dose of the implant expressed in  $\text{atoms/cm}^2$ . Values of  $R_p$ ,  $\Delta R_p$ , and related quantities have been tabulated for various ions and substrates [25]. Distortion of the profile when higher order moments are considered has also been described [25].

While the LSS theory gives fairly accurate impurity profiles for unannealed samples, the distribution can change drastically after the annealing process necessary to restructure the crystal and activate the impurities. Considerable work has been done to study how various impurities diffuse during annealing and how well the impurities are electrically and optically activated. Both of these pieces of information are essential in fabricating devices with the desired doping profiles.

The implantation process consists basically of forming a plasma containing the desired ions, accelerating the ions to a predetermined energy, selecting only the appropriate ion species out of the beam by mass separation, and directing the ions uniformly onto the substrate by scanning the beam in some manner. The charge hitting the sample is countered so that the desired dose of impurities can be obtained. A schematic diagram of the 300 keV Accelerators, Inc. 300-MP ion implanter used in this work is shown in Figure 1.1.

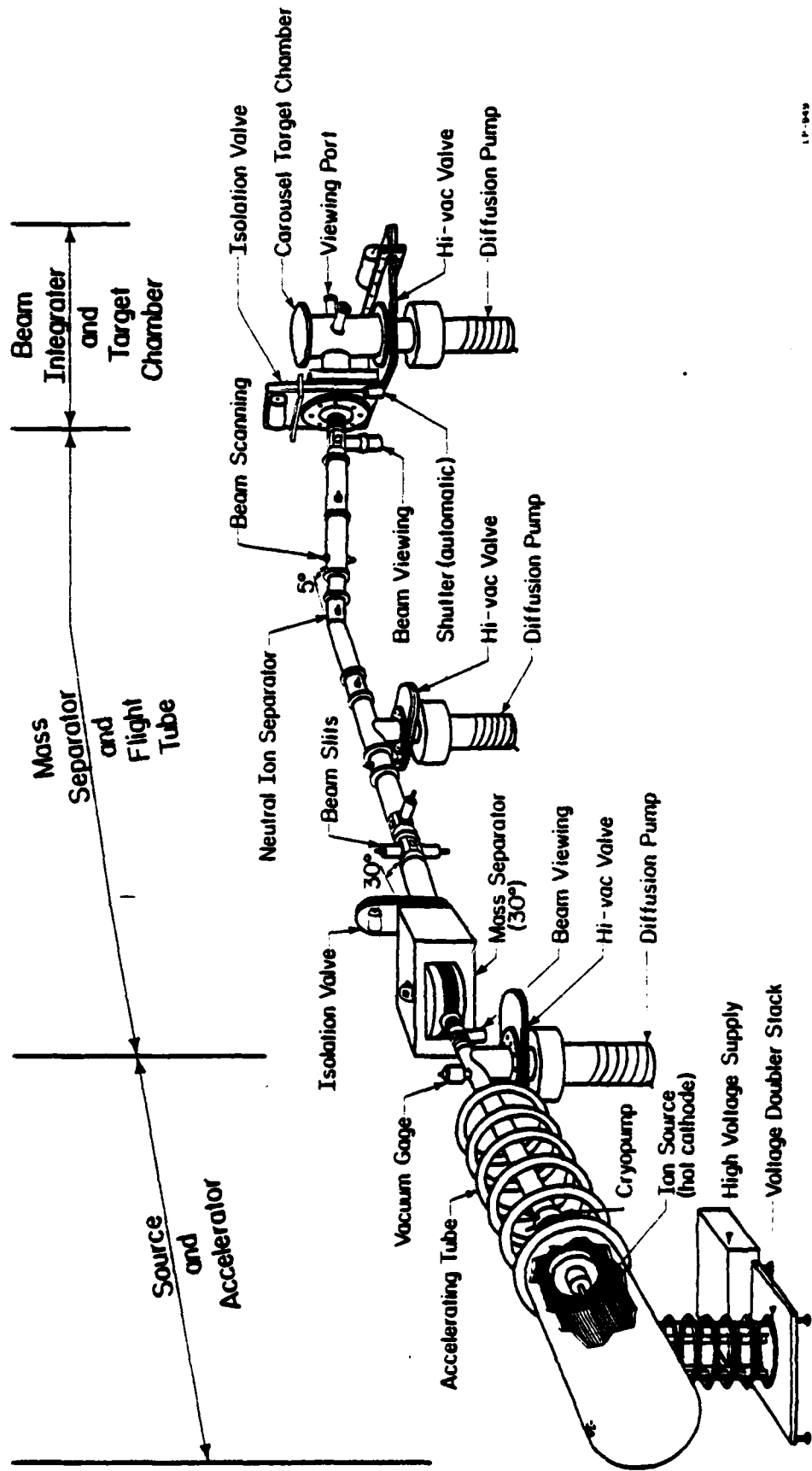


Figure 1.1. Schematic diagram of the ion implantation system.

## 2. LASER ANNEALING OF $\text{Si}^+$ IMPLANTED AMORPHIZED SILICON

In this section we study theoretically and experimentally the dynamics and quality of crystalline regrowth during annealing of multiple  $\text{Si}^+$  ion implanted amorphized silicon with a Q-switched Nd:glass laser.

Crystalline silicon can be transformed into amorphous Si by appropriate high-dose implantation [26]. There have been two models proposed to calculate the critical doses for this transformation: a critical-energy-density (CED) model [27,28], and a damage-overlap (DO) model [29,30]. Since amorphous layers play an important role in annealing behavior, the prediction of formation of amorphous Si is very important, as is its detection after implantation [31,32].

We first present theoretical results based on the thermal melting model for ion implanted amorphized silicon.

We describe the experimental set up of the Nd:glass laser system for annealing experiments.

The experimental set up for time resolved reflectivity measurements and the experimental results are then presented.

To study the quality of the crystalline regrowth we present a electron channeling pattern using a Scanning Electron Microscope.

### 2.1 Theoretical Results

A typical temperature vs. time profile for self-ion implanted amorphized silicon irradiated with a Q-switched Nd:glass laser of 50 nsec FWHM and laser fluence  $1.5 \text{ J/cm}^2$  is shown in Fig. 2.1. The shape of the laser pulse is shown in the bottom left-hand corner.  $T_m$  denotes the melting point of silicon, which is  $1685^\circ\text{K}$ . With the laser pulse, we find that the temperature at the surface rises rapidly with a parabolic trend

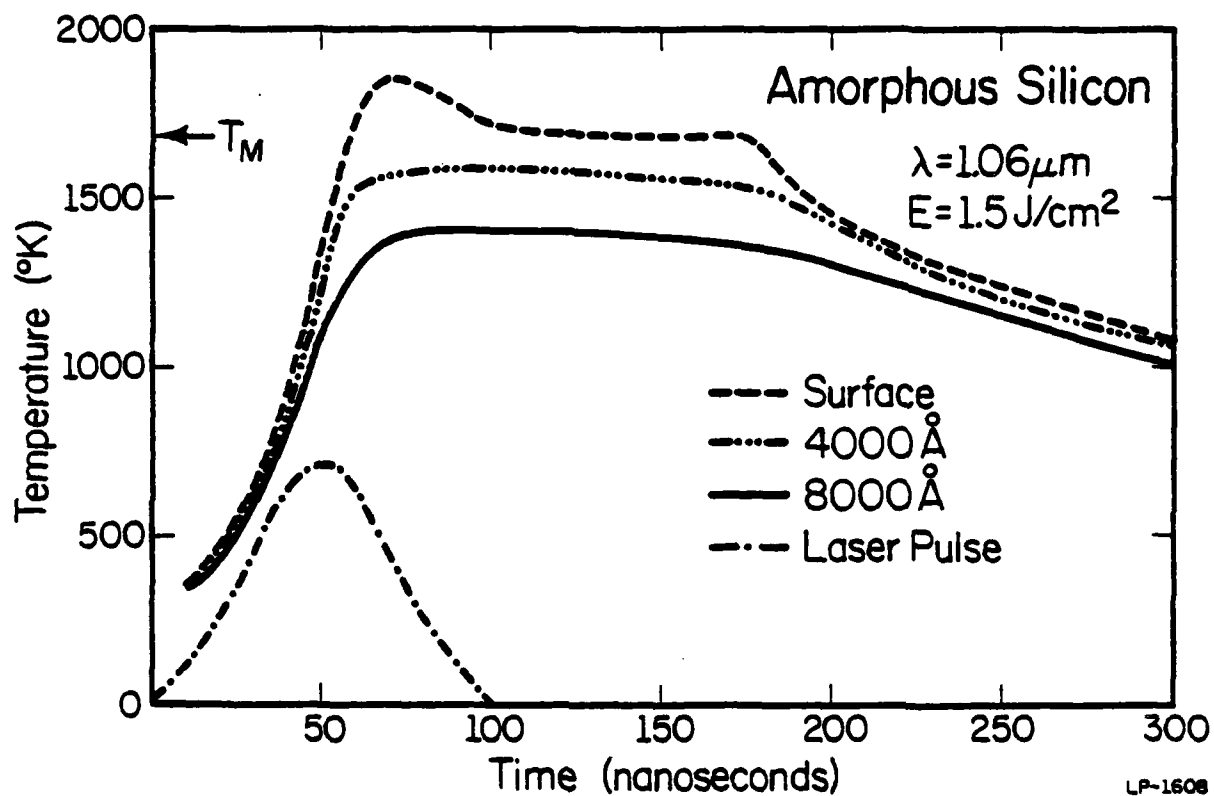


Figure 2.1. Results of the calculation showing the temperature vs. time profiles at the surface, 4000 Å, and 8000 Å layers for ion-implanted amorphized silicon irradiated with a Q-switched Nd:glass laser of fluence  $1.5 \text{ J/cm}^2$  and 50 nsecs FWHM.

until the surface melts. This is consistent with the simple phase change model as discussed by Carslaw and Jaeger [33]. The surface melts after the laser pulse reaches its peak. After melting, the temperature of the liquid rises rather sharply. The temperature profiles at depths 4000 Å are also plotted. We note that with the laser fluence of 1.5 J/cm<sup>2</sup>, the 4000 Å and 8000 Å layers never melt. Therefore, to anneal a 4000 Å amorphous layer of Si, a laser fluence of 1.5 J/cm<sup>2</sup> is not sufficient. This is confirmed by experiment. We also note that for deeper levels, the maximum temperature occurs at later times, which is expected from the mechanism of thermal diffusion of heat into the material.

In Fig. 2.2 we show a similar plot of temperature vs. time for a laser fluence of 2.0 J/cm<sup>2</sup>. In this case, the surface melts at about the peak of the laser pulse. Therefore, as the laser fluence is increased, the initiation of melting moves toward the leading edge of the pulse. Also, the temperature of the liquid rises sharply to a higher value and the surface remains molten for a longer period of time. We also note that in this case the 4000 Å layer melts, so that a liquid-phase epitaxial growth of 4000 Å thickness of amorphous silicon can be expected. This example illustrates the relevance of the model for annealing ion-implanted silicon.

Another important result of the calculation is the time evolution of the melt front into the material for a particular laser fluence. Fig. 2.3 shows the position of the melt front  $x_m$  vs. time for three different laser fluences. We note that as the laser fluence is increased, the initiation of melting occurs earlier, as expected. Also, the melt front propagates deeper into the material with increase of laser fluence. In

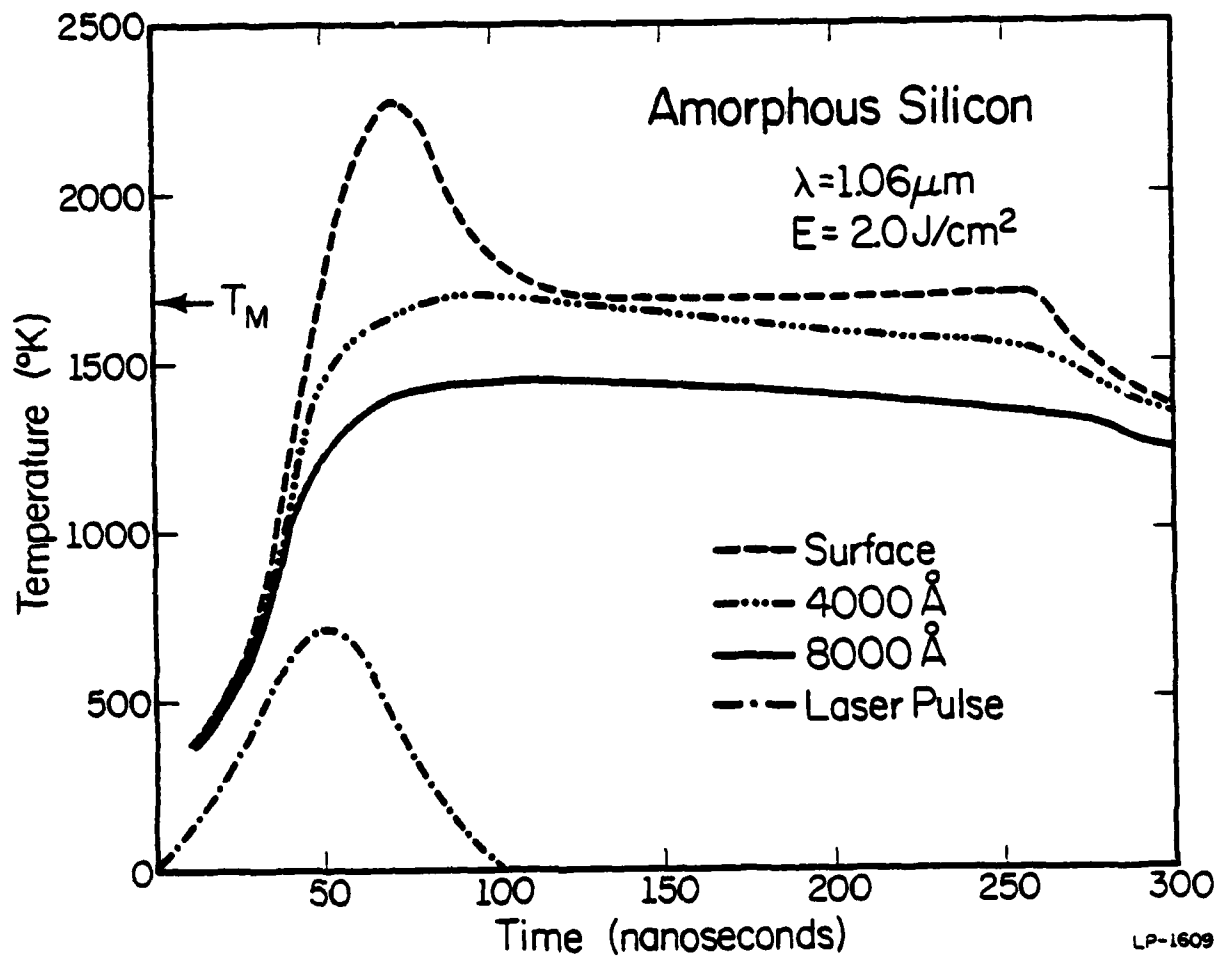


Figure 2.2. Results of the calculation showing the temperature vs. time profiles at different depths for a laser fluence of  $2.0 \text{ J/cm}^2$  (50 nsecs FWHM).

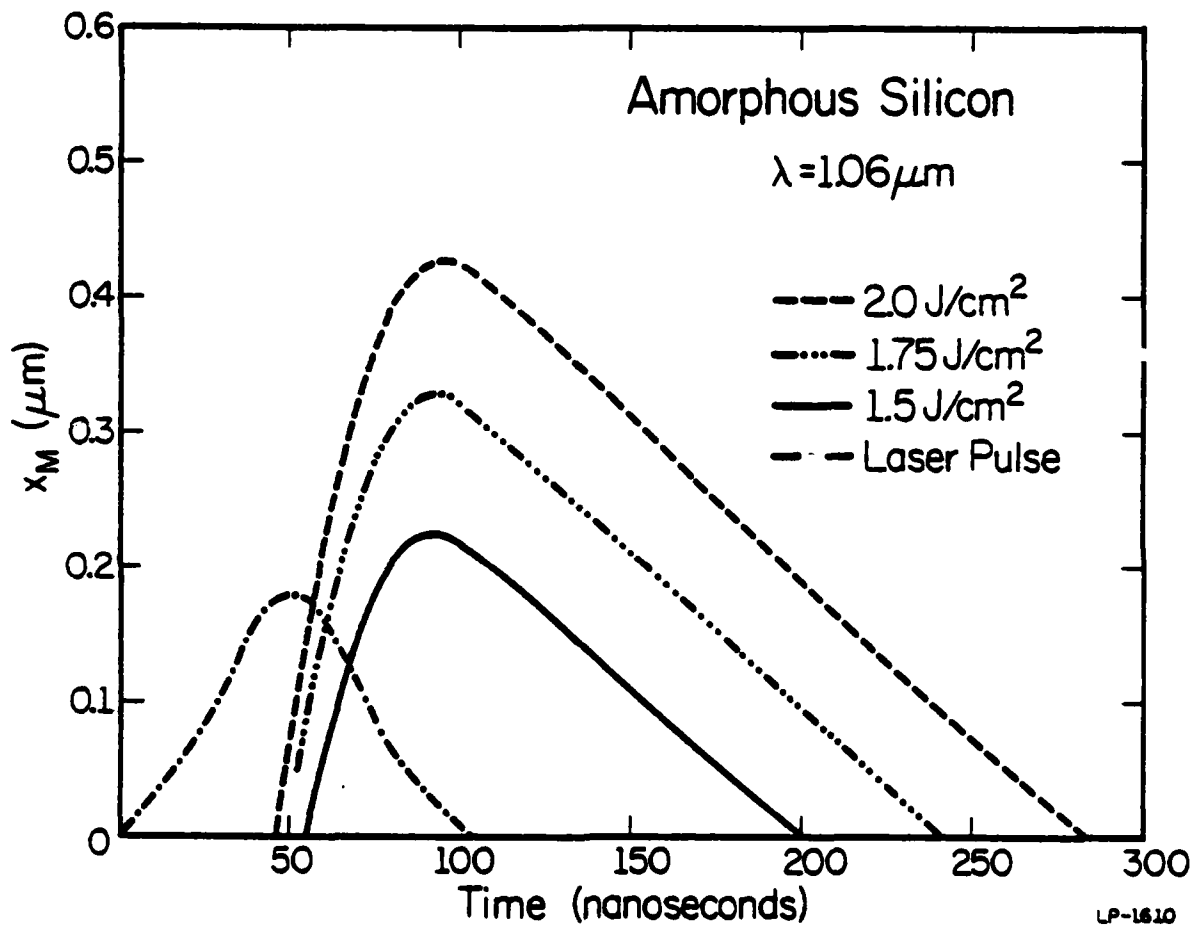


Figure 2.3. Position of the melt front vs. time for ion-implanted amorphized silicon for different laser fluences (50 nsecs FWHM).

particular, with a laser fluence of  $2.0 \text{ J/cm}^2$ , the melt front propagates to a maximum depth of about  $4000 \text{ \AA}$  into the material. The time at which the melt front reaches its maximum value shifts toward the decreasing edge of the laser pulse as the laser fluence is increased.

From Fig. 2.3 we can estimate the velocity of propagation ( $v_m$ ) of the melt front into the material and also the velocity of crystallization ( $v_c$ ) as the melt front recedes toward the surface. We find that for values of laser fluence of 1.5, 1.75, and  $2.0 \text{ J/cm}^2$ , the value of  $v_m$  is 830, 1250, 1600 cm/sec respectively. We note that with the increase of the laser fluence, the velocity of the melt front also increases. The velocity of crystallization ( $v_c$ ) for the laser fluences of 1.5,  $2.0 \text{ J/cm}^2$  are found to 225, 233, and 240 cm/sec. respectively. We observe experimentally that for a laser fluence of  $3.0 \text{ J/cm}^2$  or more there is visible surface damage.

The time during which the surface remains molten for a particular value of the laser fluence can be obtained from curves such as Fig. 2.3. For laser fluences of 1.5, 1.75, and  $2.0 \text{ J/cm}^2$ , the duration of surface melting ( $\tau_m$ ) is 145, 190, and 235 nsec, respectively. These values of  $\tau_m$  will be compared below with the experimental values obtained from the time-resolved reflectivity measurements. We note that the calculated velocity of crystallization depends sensitively on the assumed values of  $\kappa_L$  and  $\alpha_L$ . The value of  $0.322 \text{ W/cm}^\circ\text{K}$  used here [13] for  $\kappa_L$  is less than the value of  $0.50 \text{ W/cm}^\circ\text{K}$  obtained by Surko et al. [3] from electrical resistivity data using the Wiedemann-Franz law. We note that if the assumed value of  $\kappa_L$  is greater than the actual value, then the heat conduction into the material will be overestimated. The calculated surface temperature will

be too small and the maximum value of the melt depth will be too large. The increase in maximum value of  $x_m$  will increase the calculated recrystallization velocity. This is demonstrated by the fact that calculated recrystallization velocity increases with the maximum value of melt depth. Conversely, if the value of  $\kappa_L$  is underestimated, the calculated heat conduction is too small. As the silicon melts, the absorption coefficient increases rapidly, since the liquid silicon behaves like a metal. Hence, assuming a constant average value for the absorption coefficient [14] would lead to rather unjustifiable values for the velocity of crystallization.

Our calculations are in principle similar to those obtained by Bell [2]. Bell, however, assumed constant values of density  $\rho = 2.33 \text{ g/cm}^3$  and specific heat capacity  $C = 0.95 \text{ J/g-}^\circ\text{K}$  throughout the calculations. We have assumed values of density to be  $2.329 \text{ g/cm}^3$  and  $2.53 \text{ g/cm}^3$  in the solid and liquid phases respectively. Since we are considering a first order phase transition with the density  $\rho$  as the order parameter, the difference in the density between the solid and liquid phases should be taken into account. We have also considered the temperature dependence of the specific heat as it varies from a value of  $0.717 \text{ J/g-}^\circ\text{K}$  at  $300^\circ\text{K}$  to  $1.015 \text{ J/g-}^\circ\text{K}$  below the melting point. The specific heat capacity of liquid silicon is assumed to have a constant value of  $0.915 \text{ J/g-}^\circ\text{K}$ . Other than these two parameters  $\rho$  and  $C$ , the temperature and material dependence of all the parameters have been fully considered in our calculation and in those obtained by Bell.

## 2.2 Sample Preparation

To prepare self-ion implanted amorphized silicon we start with single-crystal  $2\Omega$ -cm boron-doped on  $4\Omega$ -cm phosphorus-doped silicon samples.

We choose the energies and ion doses to produce a continuous amorphous layer of  $\sim 4000 \text{ \AA}$  by using a computer program developed in our group for profile tailoring [34]. The energies and doses chosen for this work and the calculated Si implant profile are shown in Fig. 2.4. This series of  $\text{Si}^+$  implants was performed at  $\sim 163^\circ \text{ K}$  to ensure amorphization. For these low temperature implants the samples were attached to a heat sink cooled by liquid nitrogen. To reduce channeling effects, all the implantations were performed a few degrees ( $\sim 7^\circ$ ) away from the surface normal.

### 2.3 Time-Resolved Reflectivity Measurements

In studying the results of pulsed laser annealing of amorphous layers, several standard techniques such as Rutherford backscattering or transmission electron microscopy could be used to examine the quality of the crystalline regrowth mechanism itself. Since the melting model is intended to describe the dynamics of pulse laser annealing, it is useful to study the melting and regrowth as they occur. As the silicon melts during the laser pulse, the reflectivity of the surface should provide a good monitor of the phase changes [15,16]. Therefore, time-resolved reflectivity measurements were performed for comparison with the melting model.

Using a photomultiplier tube (EMI 9785 B) of risetime 1.8 nsec, we have experimentally investigated the time dependent optical reflectivity during the surface melting process (Fig. 2.5). Transitions from the amorphous to crystalline states were achieved in Si with a Nd:glass pulse of 50 nsec FWHM. The combination of high gain, low noise, and wide bandwidth makes the photomultiplier particularly useful for studying fast

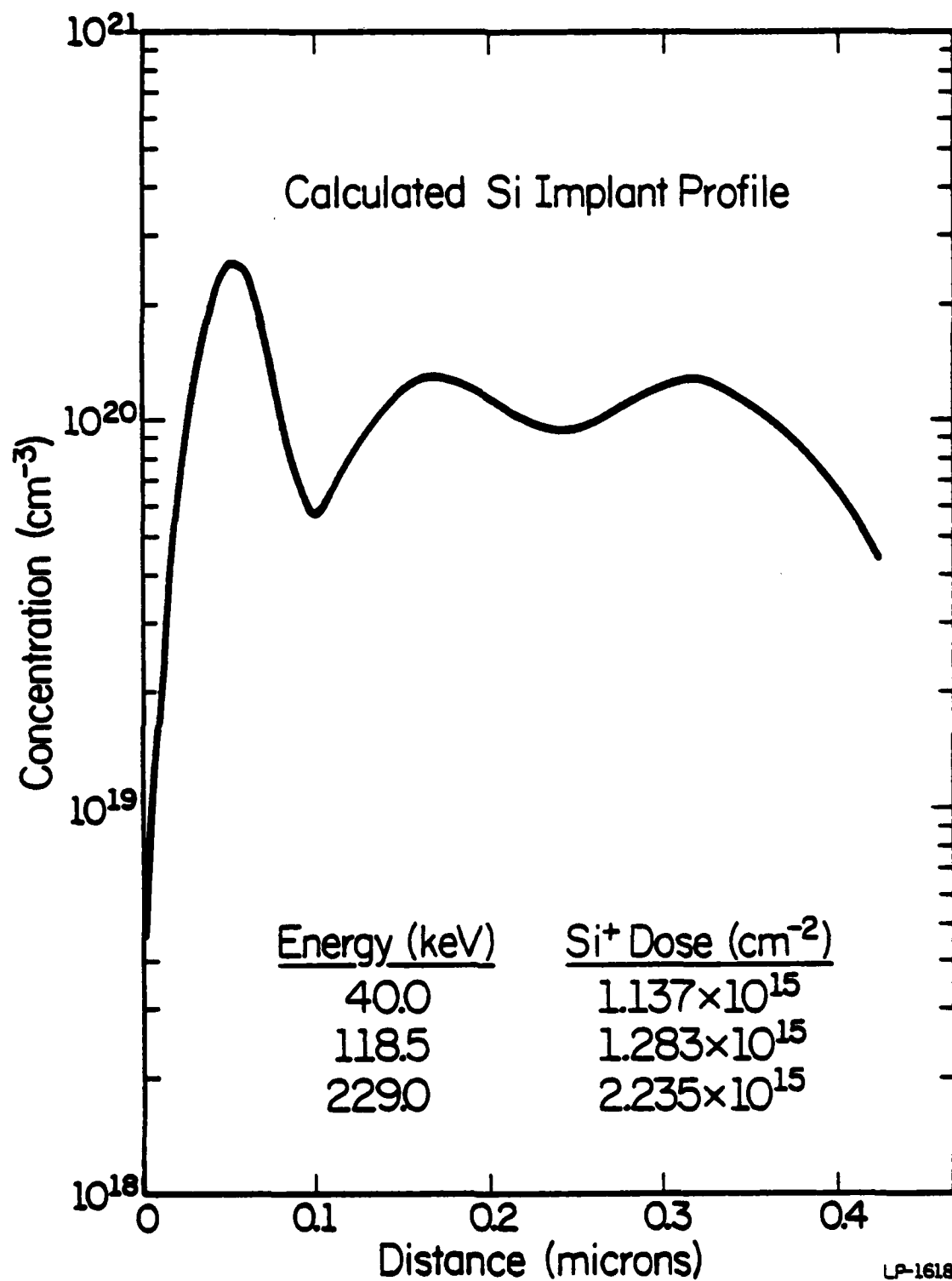
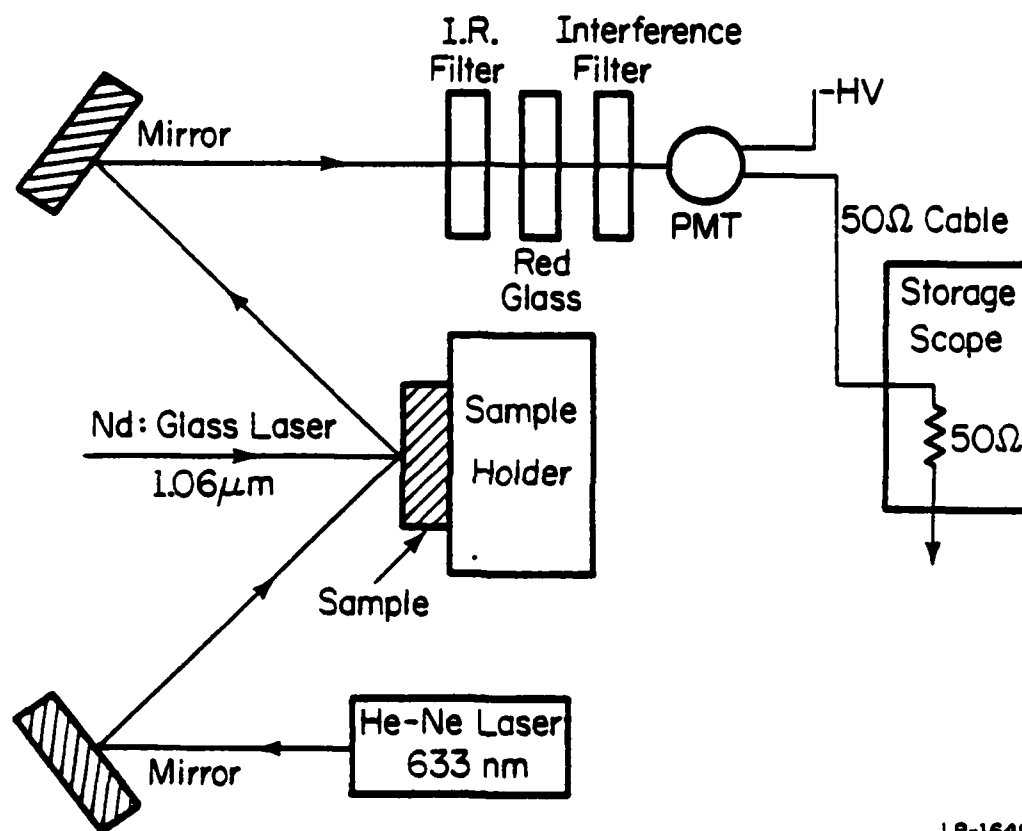


Figure 2.4. Implant concentration vs. distance as a result of three cold implants of Si<sup>+</sup> into Si to produce an amorphous layer of  $\sim 4000$  Å.



LP-1649

Figure 2.5. Experimental setup for time-dependent optical reflectivity measurements using a He-Ne laser during irradiation of the self-ion implanted amorphized silicon with a Q-switched Nd:glass laser.

transients. Johnson noise is expected to be of little consequence in typical photomultiplier-amplifier systems.

We used a 5 mW He-Ne laser operating at 633 nm and incident at  $57.5^\circ$  with the sample to study the change in reflectance during the annealing transient. The reflected light from the surface was passed through an infrared filter (3.0.D at  $1.06 \mu\text{m}$ ), a red glass (Schott G-6300) to filter out the flash lamps, and an interference filter (FWHM 7 nm) before reaching the photomultiplier tube. Transient signals displayed on the oscilloscope (Tektronix 7834) for a single pulse were recorded by a Polaroid camera.

#### 2.4 Experimental Results and Comparisons With the Melting Model

A typical reflectivity change at the surface during a  $2.0 \text{ J/cm}^2$  Nd:glass laser pulse is shown in the top frame of Fig. 2.6. The laser pulse is displayed in the bottom frame. We see that the reflectivity increases abruptly from its value for amorphous silicon at room temperature ( $\sim 40\%$ ) as the surface becomes hotter. As the laser pulse nears its peak, the front surface melts and the reflectivity rises to a value of 65%, which is consistent with the value of reflectivity for liquid silicon at 633 nm. [16]. The reflectivity stays at this value for a time given by the flat portion of the reflectivity curve. Then the reflectivity decreases and reaches a value ( $\sim 35\%$ ) corresponding to that of crystalline silicon at room temperature. For laser fluences used to observe melting of the Si surface we observe a fast rise followed by a temporary drop in reflectivity.

This drop in reflectivity suggests that the reflectivity of liquid silicon at a higher temperature than the melting point ( $1685^\circ \text{ K}$ ) is less than that of liquid silicon at the melting point. It may be speculated that this arises due to change in optical constants of liquid silicon much

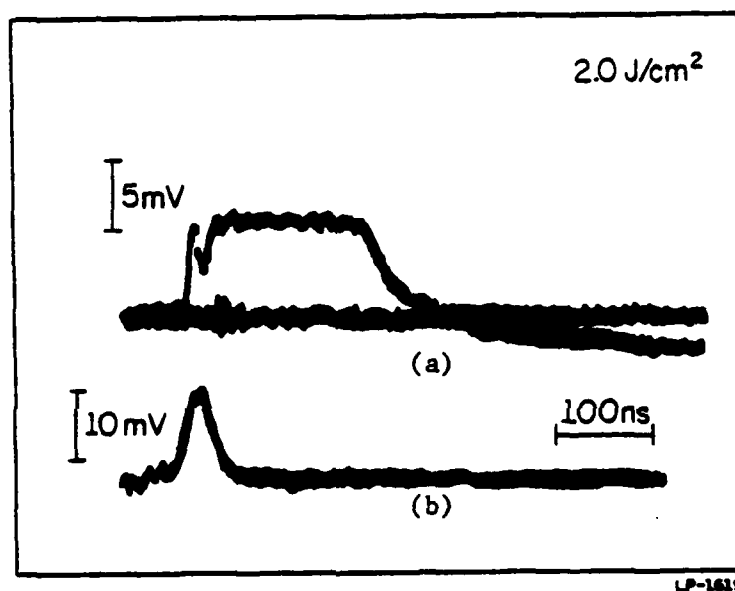


Figure 2.6. (a) Reflectivity profile of the Si surface at 633 nm as it passes through the phase transitions for a laser fluence of 2.0 J/cm<sup>2</sup>.

(b) Laser pulse (50 nsecs FWHM).

above the melting point. As our calculated temperature profile in Fig. 2.3 shows, there is an initial sharp rise in the surface temperature in the liquid phase after the front surface has reached the melting point. For the laser fluence of  $2.0\text{J}/\text{cm}^2$ , the calculated surface temperature does not rise to the boiling point ( $2953^\circ\text{K}$ ), and there is no experimental evidence of vaporization damage at  $2.0\text{J}/\text{cm}^2$ . However, for laser fluences of  $3.0\text{J}/\text{cm}^2$  and above there is visible surface damage, suggesting that the liquid silicon temperature might rise above the boiling point, leading to vaporization.

For various laser fluences, we measure the duration of the flat portion ( $\tau_m$ ) of the reflectivity curve, which gives us the time that the surface remains molten. We can then compare these values with those obtained from the plot of the time evolution of the melt front as given by Fig. 2.3. The theoretical and experimental results are shown in Fig. 2.7. We find good agreement between the theoretical predictions of the melting model and the data. We also note that the value of the reflectivity of liquid silicon does not change with the increase in pulse energy. However, for laser fluences less than the melting threshold, the reflectivity does rise to a value corresponding to that of hot silicon in the solid phase.

The onset of the reflectivity change was observed to move toward the leading edge of the pulse as the laser fluence was increased. This is also supported by the melting model as shown by Fig. 2.3. After a spot had been recrystallized, a second laser pulse of the same fluence on the same spot did not produce any change in reflectivity. This is due to the fact that the melting threshold of crystalline silicon is considerably higher than that of amorphous silicon. At the Nd:glass laser wavelength

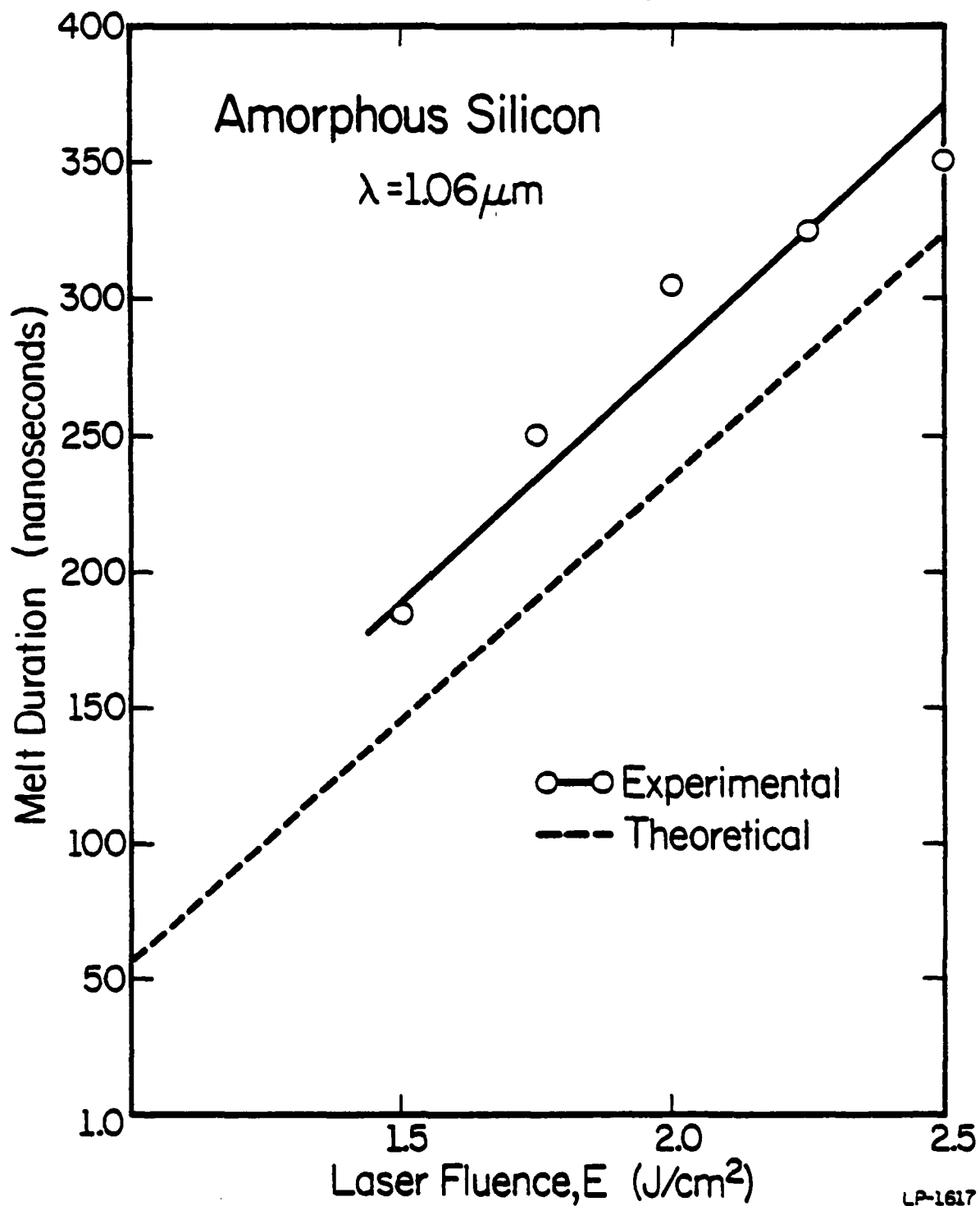


Figure 2.7. Theoretical calculations and experimental values for the melt duration vs. laser fluence during laser irradiation of self-ion implanted amorphized silicon with a Q-switched Nd:glass laser (50 nsecs FWHM).

the absorption coefficient of amorphous silicon is about a factor of 100 more than that of crystalline silicon [6]. Therefore, the amorphous sample absorbs laser energy much more efficiently prior to melting than does the crystalline silicon. This may explain observed variations of  $\tau_m$  with implantation dose [35]. For laser fluences greater than the damage threshold ( $\sim 3.0 \text{ J/cm}^2$ ), we find an irreversible decrease in reflectivity due to surface damage.

Also from Fig. 2.6 we see that after the molten period ( $\tau_m$ ) the reflectivity of the surface decreases as the surface cools and eventually reaches the value of that of crystalline Si at room temperature. We note that initially we have amorphous silicon of reflectivity 40% at room temperature and finally we have crystalline silicon of reflectivity 35% at room temperature. The observed change in surface reflectivity before and after the experiment is consistent with the phase transition from amorphous to crystalline material.

### 2.5 Electron Channeling Pattern Using a Scanning Electron Microscope

When a parallel electron beam rocks about a spot on the specimen surface, the number of backscattered electrons varies according to the correlation between the incident beam and the crystal orientation of the specimen. Let us assume that a particular set of crystal planes satisfies the Bragg diffraction condition,

$$2d \sin \theta = n\lambda \quad (2.1)$$

where  $d$  is the interplanar spacing,  $\theta$  is the angle between the beam and the planes, and  $\lambda$  the electron wavelength.

In this case, the penetration depth of the incident beam into the specimen varies, and thus the intensity of the backscattered electrons

varies with respect to the beam incidence angle. Accordingly, if the incident beam is angle-scanned in two directions, various pairs of parallel lines referred to as the Electron Channeling Pattern appear on the cathode ray tube. These lines correspond to the lattice planes having various spacings in the crystal.

To investigate the material properties of the amorphized layer before and after the laser pulse, we employed the technique of electron channeling using a scanning electron microscope. For the as-implanted material there was no electron channeling pattern, confirming the presence of an amorphous layer. The sample which was irradiated with a  $2.5 \text{ J/cm}^2$  laser fluence clearly showed an electron channeling pattern due to the crystalline regrowth of the amorphous layer. The regrown layer has a  $\langle 100 \rangle$  orientation, as expected for recrystallization on the  $\langle 100 \rangle$  substrate. A typical picture of the channeling pattern is shown in Fig. 2.8.

The channeling pattern shown in Fig. 2.8 is as sharp as that obtained from an unimplanted sample from the same wafer. This supports the fact that a fluence of  $2.5 \text{ J/cm}^2$  is sufficient for the melt-front to move through the original amorphous-crystalline interface, as predicted from the calculations.

Nd: Glass Laser  
2.5 J/cm<sup>2</sup>

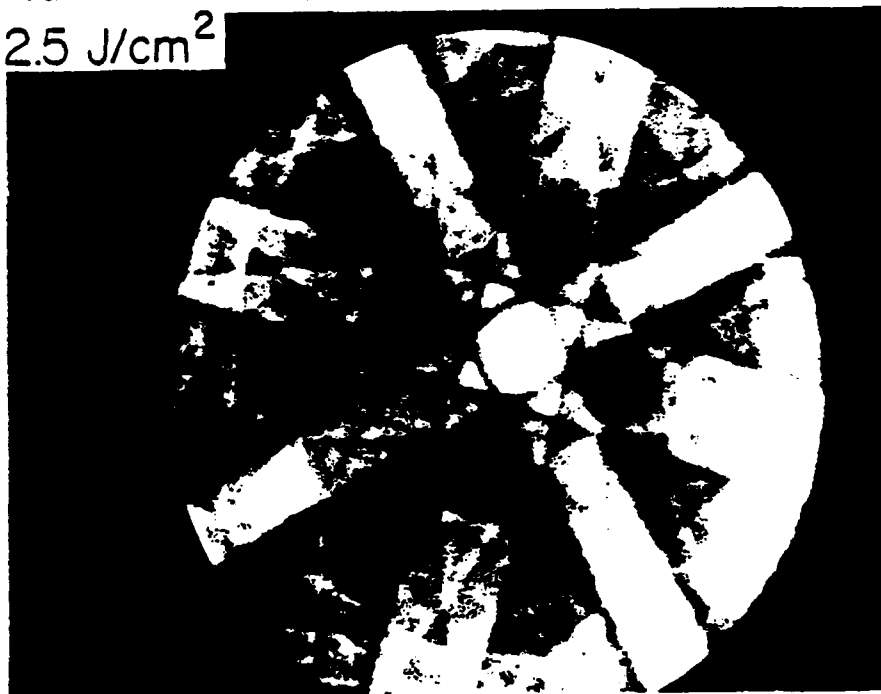


Figure 2.8. Electron channeling pattern of the Si<sup>+</sup> implanted amorphized Si <100> after irradiation with a laser pulse of 2.5 J/cm<sup>2</sup>.

### 3. LASER ANNEALING OF $\text{BF}_2^+$ IMPLANTED AMORPHIZED SILICON

Pulsed laser annealing has been suggested as a method to process semiconductor devices fabricated by ion implantation. In the fabrication of electronic devices in Si, the use of high-dose implantation is often necessary. Such implantation produces an amorphous layer of a few thousand angstroms on the silicon surface. The recrystallization of such amorphous layers during pulsed laser annealing and the accompanying electrical activation are not only of interest fundamentally, but also are important to device fabrication. The physical mechanism behind the laser-semiconductor interaction leading to crystalline growth and electrical activation of dopant atoms is based on a thermal melting model [36, 2].

The implantation of  $\text{BF}_2$  molecular ions into Si is a useful method for acceptor doping, in which B provides the dopant and F accomplishes the amorphization [31]. The range statistics for molecular ion ( $\text{BF}_2^+$ ) implants can be predicted by assuming that the  $\text{BF}_2$  molecule splits into its components with energies apportioned by mass ratio. For example, a 150 keV  $\text{BF}_2$  molecule results in two  $^{19}\text{F}$  with 58 keV and one  $^{11}\text{B}$  with 34 keV in the Si sample.  $\text{BF}_2$  implanted Si, with fluence  $\geq 1 \times 10^{15}/\text{cm}^2$ , has high electrical activation after low-temperature thermal annealing, and p<sup>+</sup>-n junctions formed by  $\text{BF}_2^+$  implants have low reverse leakage current. For the fabrication of devices requiring shallow p regions,  $\text{BF}_2^+$  is easier to implant than  $\text{B}^+$ , since the implantation energy for  $\text{BF}_2^+$  is much larger than that for  $\text{B}^+$  to form identical boron range distributions, and more stable ion beam currents can therefore be obtained for  $\text{BF}_2^+$  implants. Another advantage of  $\text{BF}_2^+$  implantation is the amorphization provided by the heavier fluorine atom. Conventional thermal annealing at  $\sim 550^\circ\text{C}$  results in

regrowth of the amorphized layer, but does not electrically activate the tail of the B distribution, located below the original amorphous-crystalline interface [31]. Only in a thicker amorphous layer, formed for example by multiple  $\text{Si}^+$  predamage implants, can the entire B profile be activated [31].

We have used the technique of pulsed laser annealing to electrically activate the B distribution by liquid phase epitaxial regrowth, thereby avoiding the complication of implanting B into a thicker amorphous layer produced by  $\text{Si}^+$  implants. The laser fluence corresponding to the melting threshold is determined experimentally by time-resolved reflectivity measurements [36, 37]. The boron atomic distributions are determined by the SIMS technique. Differential resistivity and Hall effect measurements in conjunction with successive layer removal are used to obtain the electrical carrier distributions as a function of the laser fluence. We find that to obtain full electrical activation, the depth of melting must exceed the extended tail of the defect distribution, which is much deeper than the calculated value. The presence of such an extended defect distribution has been attributed to enhanced diffusion and partial channelling [38].

### 3.1 Theoretical Results

The details of the melting model have been discussed in Chapter 1. The laser light is absorbed in the near surface region of the solid. The power absorbed by the solid can be expressed by a source term which is both spatial and time dependent. The absorbed light energy is then converted into heat, which diffuses into the bulk by thermal conduction. This process can be explained by considering the one-dimensional heat conduction equation

with an appropriate source term given by

$$C(T)\rho\frac{\partial T}{\partial t} = \frac{\partial}{\partial x} (\kappa(T) \frac{\partial T}{\partial x}) + S(x,t) \quad (3.1)$$

where  $\kappa$  is the thermal conductivity,  $C$  is the specific heat capacity, and  $\rho$  is the density of the material. The source term  $S$  is governed by the mechanism of the laser-solid interaction and the time shape of the laser pulse. The laser pulse is assumed to be Gaussian with FWHM = 27.5 ns. The source term is given by

$$S(x,t) = \frac{1}{\pi^{1/2}\Gamma} \exp\left(-\frac{(t-t')^2}{\Gamma}\right) E(1-R) \alpha e^{-\alpha x} \quad (3.2)$$

where  $\Gamma$  is the full width duration of the pulse at  $1/e$  intensity,  $t'$  is the time when the pulse reaches its maximum value,  $E$  is the laser fluence in  $J/cm^2$ ,  $R$  is the reflection coefficient, and  $\alpha$  is the absorption coefficient. After the front surface has melted, the heat flow into the liquid is described by an equation similar to (3.1), with parameters appropriate for the liquid phase.

We have used the technique of finite difference equations to solve the nonlinear heat conduction equations for the solid and liquid phases, taking into account appropriate time-dependent boundary conditions for finding the position of the melt-front as a function of time. We have considered the temperature variation of thermal conductivity and specific heat capacity of Si in the solid and liquid phases. The density of Si in the solid and liquid phases is  $2.33 \text{ g/cm}^3$  and  $2.53 \text{ g/cm}^3$ , respectively. For the case of a Nd:glass laser ( $\lambda = 1.06 \text{ }\mu\text{m}$ ), the values of the reflection coefficient in the solid and liquid phases are 0.31 and 0.76, respectively.

This large change in the value of reflectivity during phase transitions was considered throughout the calculations and was monitored experimentally during time-resolved reflectivity measurements.

At 1.06  $\mu\text{m}$ , the value of the absorption coefficient of amorphous Si is  $6 \times 10^3/\text{cm}$ . Since the implanted amorphous layer is  $\sim 1325 \text{ \AA}$  thick, we have considered the substrate effects, especially the marked difference between the absorption coefficients of amorphous and crystalline Si at 1.06  $\mu\text{m}$ . The absorption coefficient of the crystalline substrate depends markedly on temperature arising from the interband absorption and free-carrier absorption [39]. The  $\alpha$  for crystalline Si varies from  $14.5/\text{cm}$  at  $300^\circ\text{K}$  to  $4.7 \times 10^3/\text{cm}$  at the melting point ( $1685^\circ\text{K}$ ). This variation of  $\alpha$  can be fitted to an empirical relation  $\alpha (\text{c-Si}) = 1.35 \times 10^{-7} T^{3.32}/\text{cm}$  [40]. For a realistic model dealing with a thin amorphous layer of thickness much smaller than  $\alpha^{-1}$ , it is crucial to take this temperature dependent  $\alpha$  for c-Si into account. In his calculations, Bell [2] assumed a constant value of  $100/\text{cm}$  for absorption coefficient of the crystalline substrate. Such an average value for  $\alpha$  does not reflect the dynamics of the processes arising from interband and free-carrier absorption processes. However, when the amorphous layer is thick enough ( $> \alpha^{-1}$ ), one can neglect the substrate effects without much loss of accuracy. The absorption coefficient of liquid Si at 1.06  $\mu\text{m}$  is assumed to be  $1.4 \times 10^6/\text{cm}$ .

In Fig. 3.1 we have plotted the temperature at the surface and at various distances inside the Si at different times for a fluence of  $2.5 \text{ J/cm}^2$ . At 10 ns, the temperature profile is very flat indicating that the temperature rise is being governed by adiabatic processes. The temperature profile becomes sharper as time increases, as shown by the profile at 20 ns, as thermal diffusion processes become more important. At 37.5 ns, the surface

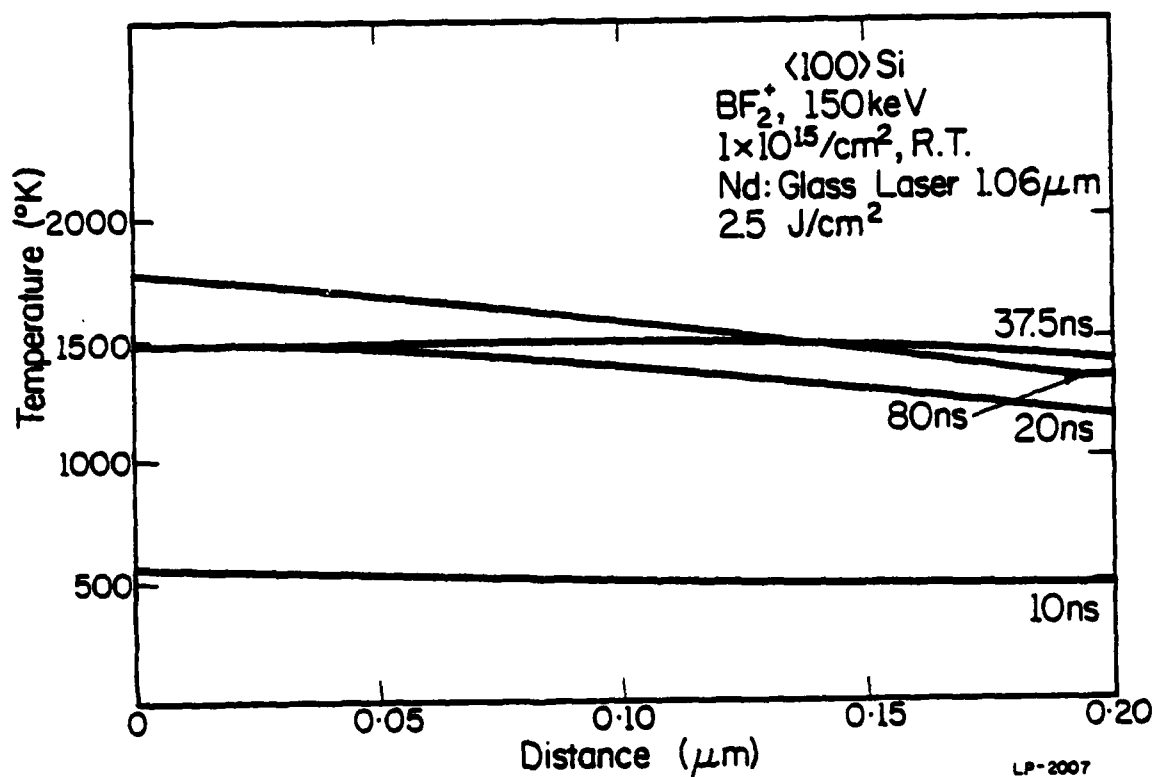


Figure 3.1. Results of the calculation showing the temperature vs. distance profiles at various times for a laser fluence of  $2.5 \text{ J/cm}^2$  (27.5 ns FWHM).

temperature rises to its maximum value of 1780 K and the gradient in the temperature profile is maximum. At later times (e.g., 80 ns) the profile becomes very flat as the temperature remains constant at the melting point of a-Si to a depth of  $\sim 1400 \text{ \AA}$ .

In Fig. 3.2 we show the time evolution of the melt front ( $x_m$ ) for three different laser fluences. We note that as the laser fluence is increased, the initiation of the melting occurs earlier, as expected. Also, the melt front propagates deeper into the material with increase of laser fluence. In particular, with a laser fluence of  $3.0 \text{ J/cm}^2$ , the melt front propagates to a maximum depth of  $2800 \text{ \AA}$  into the material, which is more than the thickness ( $1325 \text{ \AA}$ ) of the implanted amorphous region.

From Fig. 3.2 we can estimate the velocity of propagation ( $v_m$ ) of the melt front into the material and also the velocity of crystallization ( $v_c$ ) as the melt front recedes towards the surface. We find that for values of fluence of 2.0, 2.5, and  $3.0 \text{ J/cm}^2$ , the value of  $v_m$  is 535, 600, and 950 cm/sec respectively. We note that with the increase of the laser fluence, the velocity of the melt front also increases. The velocity of crystallization ( $v_c$ ) from the laser fluences of 2.0, 2.5, and  $3.0 \text{ J/cm}^2$  are found to be 90, 95, and 100 cm/sec, respectively.

In Fig. 3.3 we plot the duration of the surface melting and the maximum depth of the melt front as a function of the laser fluence.

From time-dependent reflectivity measurements we found that the threshold for melting is  $1.0 \text{ J/cm}^2$ . We have adjusted the value of the absorption coefficient of the implanted layer such that the calculated value of the threshold laser fluence for melting is also  $1.0 \text{ J/cm}^2$ . From Fig. 3.3 we find that the laser fluence necessary to melt  $1325 \text{ \AA}$  is  $2.3 \text{ J/cm}^2$ .

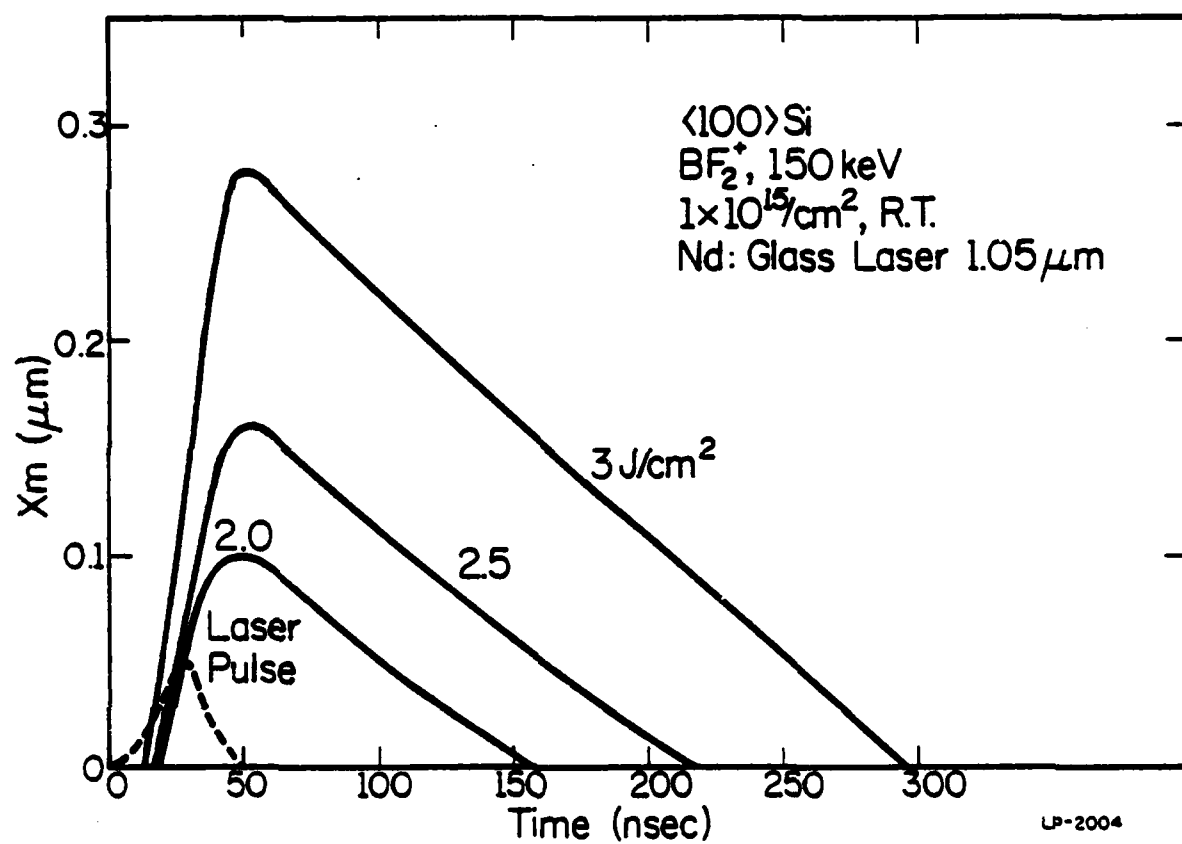


Figure 3.2. Position of the melt front vs. time for different laser fluences (27.5 ns FWHM).

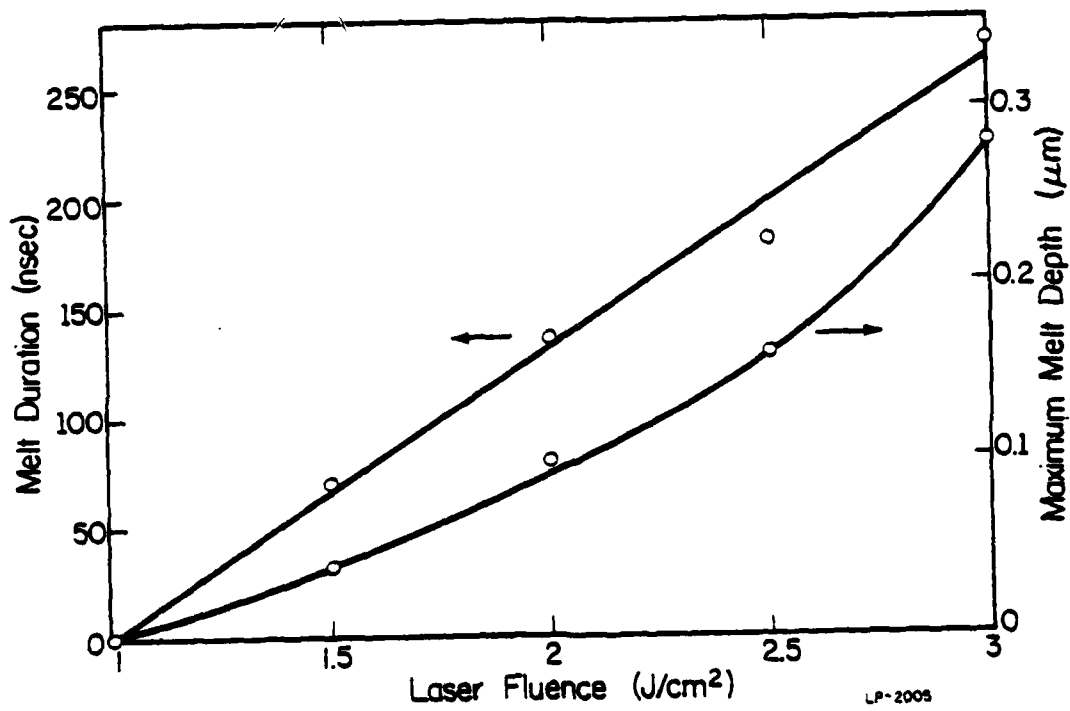


Figure 3.3. Calculated values of the duration of surface melting and the maximum depth of the melt front vs. laser fluence.

### 3.2 Sample Preparation

Wafers of 4  $\Omega$ -cm phosphorus-doped <100> silicon were used in this investigation.  $\text{BF}_2^+$  was implanted at room temperature at 150 keV to a dose of  $1 \times 10^{15}/\text{cm}^2$ . To reduce channeling effects, the implantations were performed a few degrees ( $\sim 7^\circ$ ) away from the surface normal. This implantation produced an amorphous layer of thickness  $\sim 1325$  Å, as determined by HF etching experiments [31].

### 3.3 Time Resolved Reflectivity Measurements

The details of the experimental set up for doing time-resolved reflectivity measurements has been described in Chapter 2.3. In this case we used a 5W Ar laser operating at 488 nm and a 5 mW He-Ne laser operating at 633 nm incident on the sample to study the change in reflectance during the annealing transient. A 400 MHz Tektronix transient digitizer was used to record the transient signals.

A typical reflectivity change at the surface probed by an Ar laser (488 nm) during a  $4.0 \text{ J}/\text{cm}^2$  Nd:glass laser pulse is shown by the solid line in Fig. 3.4. The laser pulse is indicated by the dashed line. We see from Fig. 3.4 that the reflectivity increases abruptly from its value for amorphous silicon at room temperature ( $\sim 40\%$ ) to a value of 66% corresponding to the value of liquid silicon at 488 nm [16]. The value of reflectivity remains at 66% during the molten period (180 ns), and then decreases to a value of 35% corresponding to crystalline Si at room temperature. For various laser fluences, and using the Ar and He-Ne probe lasers, we measured the duration of the flat portion ( $\tau_m$ ) of the reflectivity curve, which gives the time that the surface remains molten. Fig. 3.5 shows the

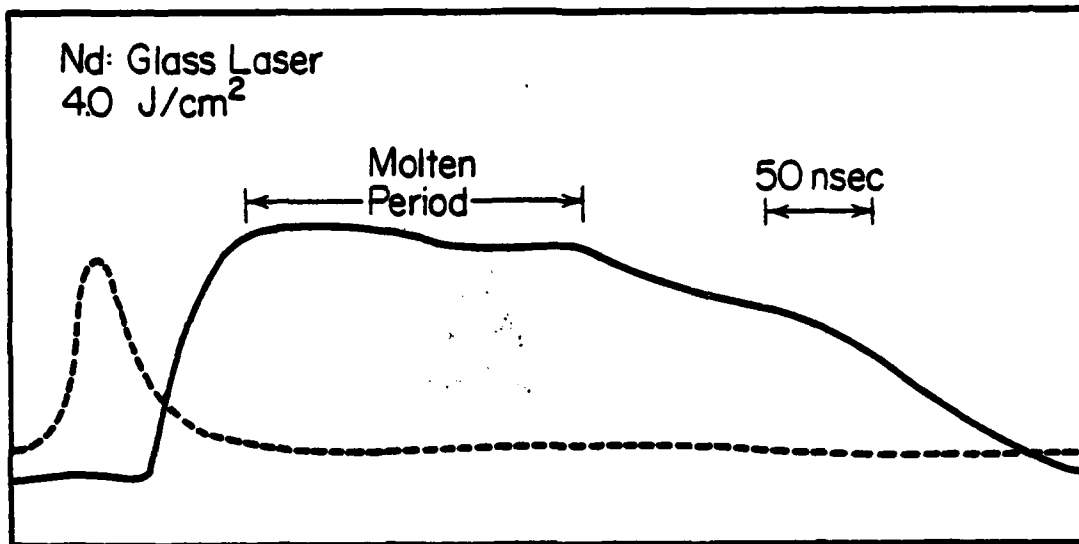


Figure 3.4. Reflectivity profile (solid line) of the Si surface at 433 nm as it passes through the phase transition for a Nd:glass laser fluence of 4.0 J/cm<sup>2</sup>. The dashed line shows the laser pulse (27.5 ns FWHM).

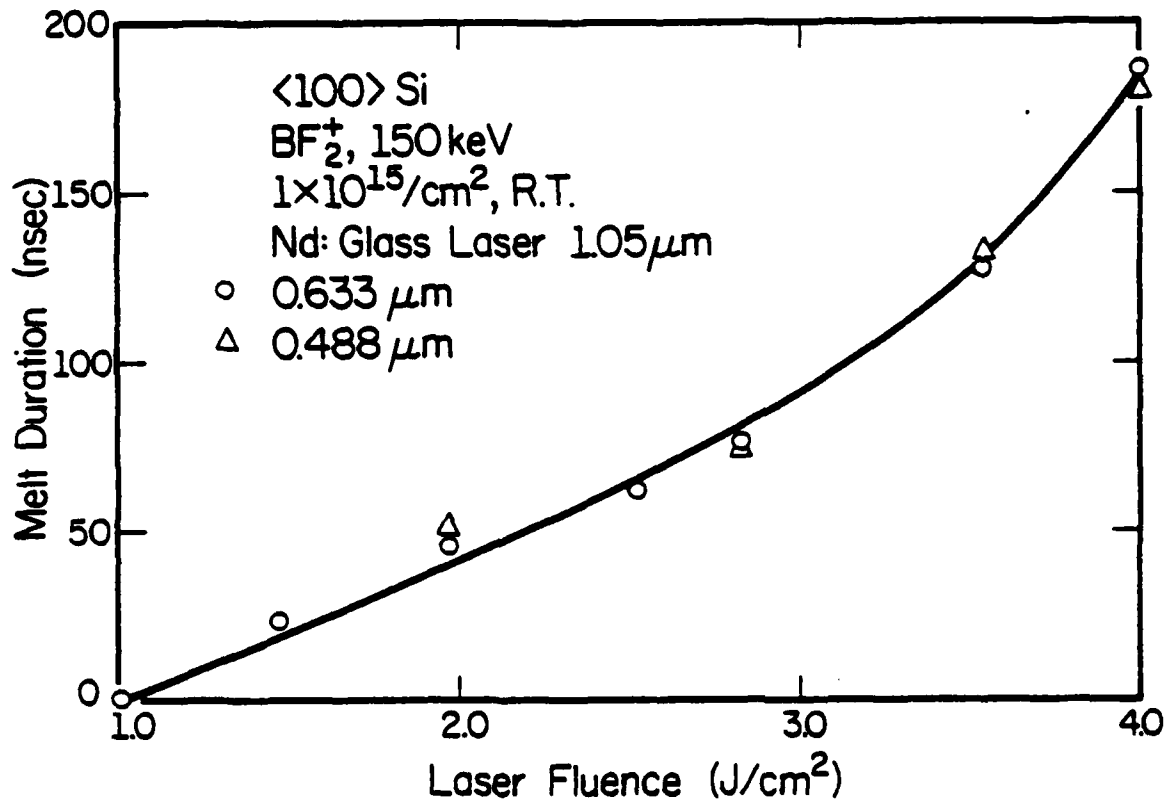


Figure 3.5. Duration of surface melting ( $\tau_m$ ) vs. laser fluence as monitored by an Ar laser and a He-Ne laser.

plot of experimentally determined values of  $\tau_m$  vs. laser fluence.

There have been speculations by Van Vechten et al. [7] that the phenomenon of pulsed laser annealing is a nonthermal process resulting from the presence of a dense plasma of photoexcited carriers. As discussed by Nathan et al. [9] the plasma model would predict a probe wave-length dependence of  $\lambda^4$  for the measured melt-duration  $\tau_m$ . However, we find that the measured duration of surface melting  $\tau_m$  is independent of the wave-length of the probe laser. The plasma model prediction can be summarized by the relation  $\tau_m(488 \text{ nm}) = 0.35 \tau_m(633 \text{ nm})$ . Since our experimental results conclusively show that  $\tau_m$  is independent of wavelength as probed by the Ar or He-Ne lasers, the melting model properly explains the dynamics of surface melting and crystalline regrowth during the pulsed laser annealing studied here.

The melting threshold was experimentally determined to be larger than  $1.0 \text{ J/cm}^2$ . Samples were annealed with laser fluences of 1.0, 2.0, 2.5, 3.54, and  $4.0 \text{ J/cm}^2$  for study with the SIMS and the Hall effect measurements.

### 3.4 Atomic Profiling

The boron, fluorine atomic profiles presented in this work were measured by secondary ion mass spectrometry (SIMS) [41, 42] using a CAMECA IMS-37 ion microprobe located in the Materials Research Laboratory. In this measurement technique, an  $\text{O}_2^+$  primary beam was rastered over an area of  $\sim 250 \mu\text{m}^2$ . Standard precautions were taken to reject spurious signals from the crater walls. The  $^{11}\text{B}$  and  $^{19}\text{F}$  sputtered ion intensities were normalized to the intensity of  $^{30}\text{Si}$  sputtered ions from the matrix to compensate for changes in the secondary ion interaction efficiency as different specimens

were moved into the analysis position of the ion microscope. Depth scales were determined by crater depth measurements using a Dektak stylus. The concentration scale was obtained from a standard prepared by implanting  $\text{BF}_2^+$  into Si to a dose of  $1 \times 10^{15}/\text{cm}^2$  at 150 keV, and measuring the unannealed profile.

Figure 3.6 shows a plot of the boron atomic concentration as determined by SIMS measurements for the as-implanted sample and for samples annealed with laser fluences of 1.0, 2.0, 2.5, 3.5 and  $4.0 \text{ J}/\text{cm}^2$ . For the laser fluence of  $1.0 \text{ J}/\text{cm}^2$ , no melting was observed by time-resolved reflectivity measurements. The boron atomic profile for  $1.0 \text{ J}/\text{cm}^2$  laser fluence is identical to that of the as-implanted sample. Since there is no melting at  $1.0 \text{ J}/\text{cm}^2$ , there is no redistribution of the implanted profile, due to the small diffusion coefficient of boron in the solid phase ( $\sim 10^{-14} \text{ cm}^2 \text{ s}^{-1}$ ).

For laser fluences of 2.0, 2.5, 3.5 and  $4.0 \text{ J}/\text{cm}^2$  there is an increasing redistribution of the boron atomic profile with increase of the laser fluence. The substitutional redistribution of boron induced by pulsed laser annealing as shown by Figure 3.6 cannot be explained by thermal diffusion in the solid because the time scale is too short. Since the melt duration is on the order of a few hundred nanoseconds, this redistribution of the boron atomic profile can only be attributed to diffusion in the liquid phase [4]. The diffusion coefficient of boron in the liquid phase is  $\sim 10^4 \text{ cm}^2 \text{ s}^{-1}$ . As the laser fluence is increased beyond the melting threshold of  $1.0 \text{ J}/\text{cm}^2$ , boron diffuses deeper into the material and the profile becomes flatter as shown in Figure 3.6. The SIMS results shown in Fig. 3.6 directly support the thermal melting model.

Figure 3.7 shows a plot of the fluorine atomic concentration as

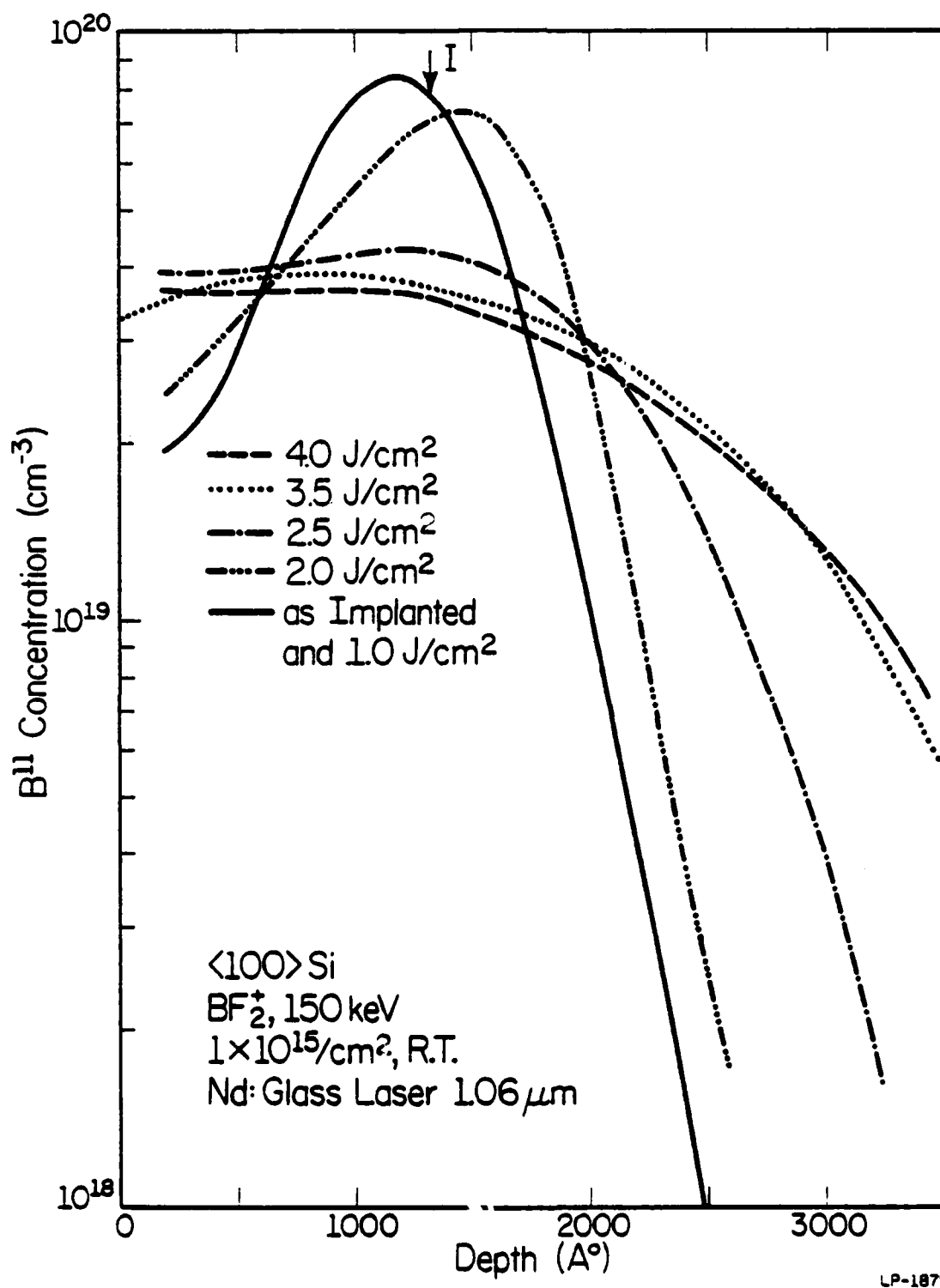


Figure 3.6. Boron atomic concentration for the as-implanted sample and for samples irradiated with various laser fluences. The implanted amorphous crystalline interface is denoted by I.

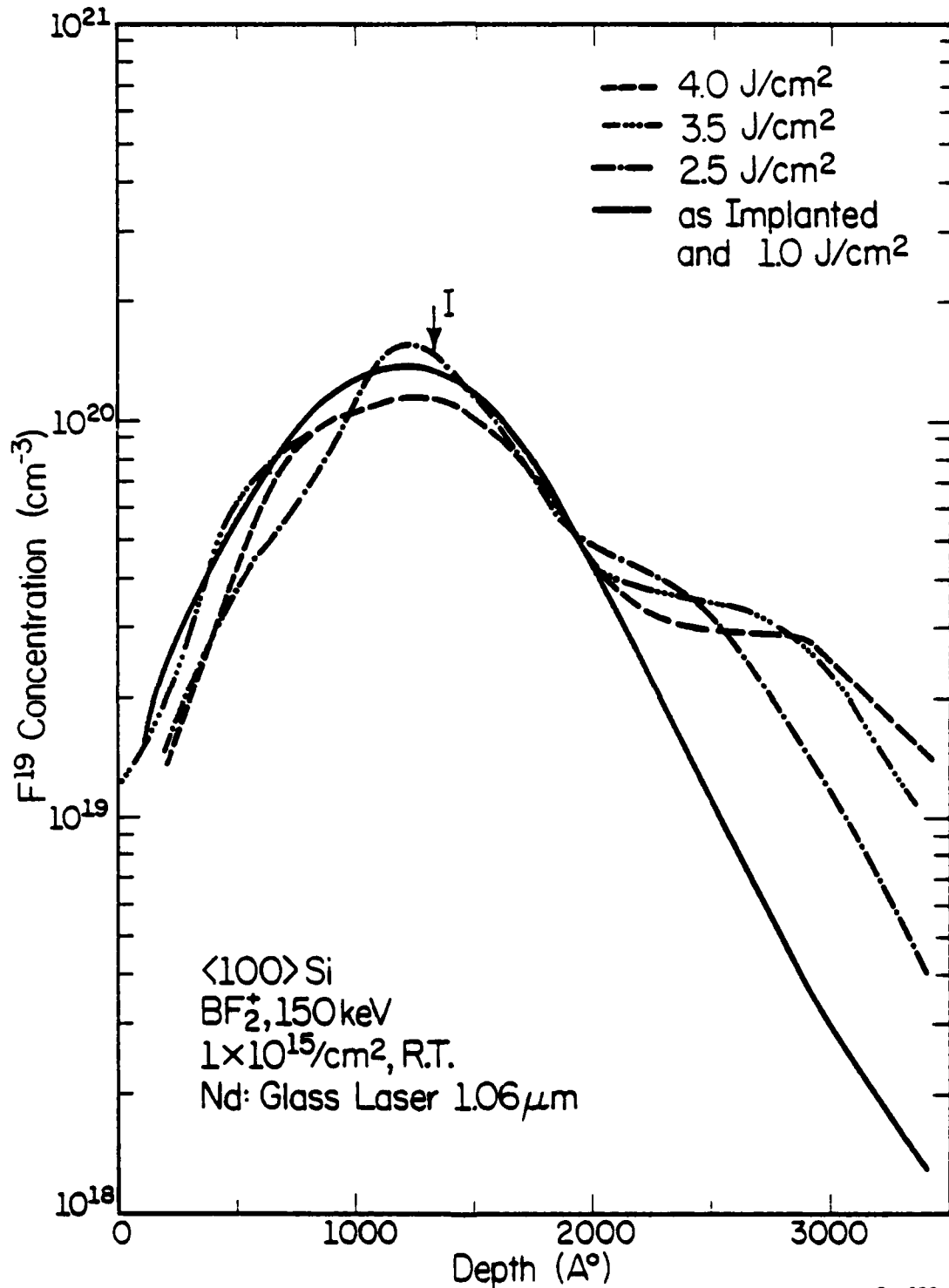


Figure 3.7. Fluorine atomic concentration for the as-implanted sample and for samples irradiated with various laser fluences. The implanted amorphous-crystalline interface is denoted by I.

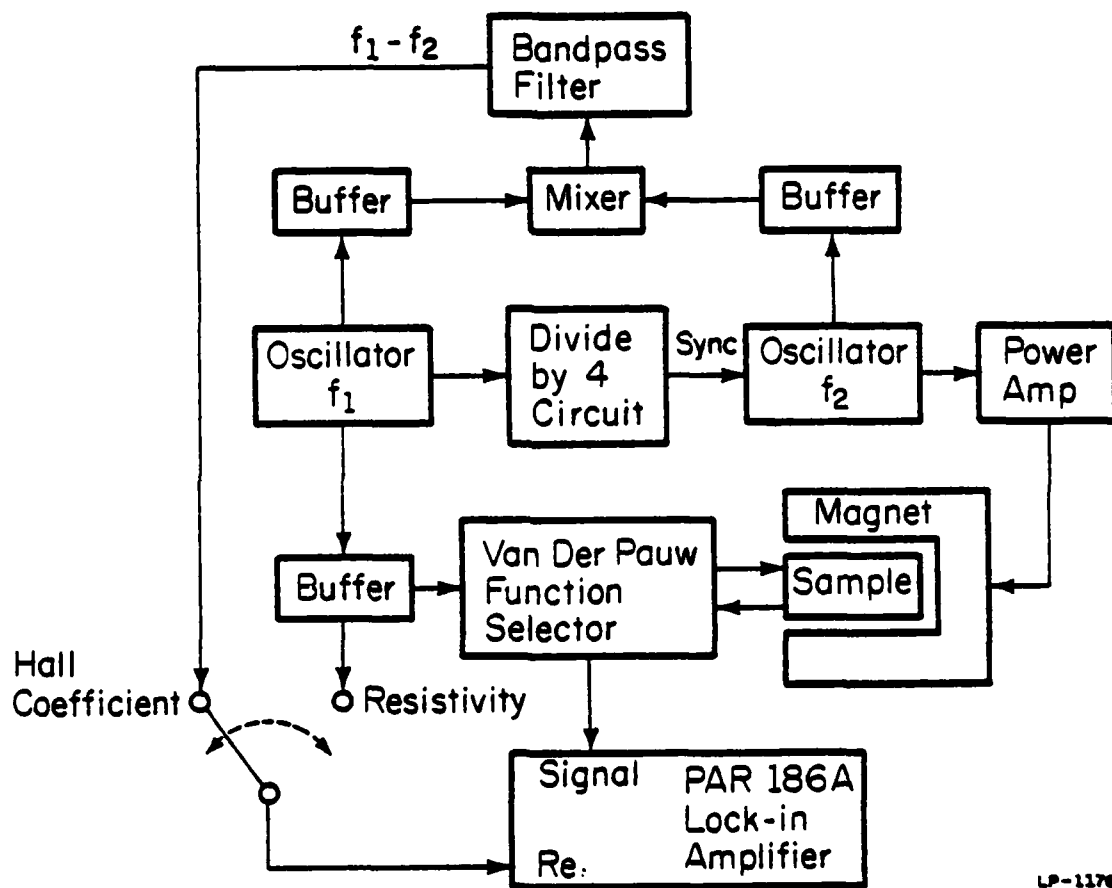
determined by SIMS measurements for the as-implanted sample and for samples annealed with laser fluences of 1.0, 2.5, 3.5 and 4.0 J/cm<sup>2</sup>. The profiles for the as-implanted and the 1.0 J/cm<sup>2</sup> samples are identical, since there is no melting. The most significant changes in the fluorine profiles are the appearance of pronounced shoulders in the profiles at ~ 2250 Å (for 2.5 J/cm<sup>2</sup>), ~ 2500 Å (for 3.5 J/cm<sup>2</sup>) and ~ 2700 Å (for 4.0 J/cm<sup>2</sup>). Apparent changes in the fluorine concentration near the peak of the profile may be within the experimental uncertainties of the SIMS technique. The redistribution of fluorine will be considered below along with the electrical activation of the boron atoms.

### 3.5 Electrical Profiling

To investigate the electrication activation after pulsed laser annealing we determine the sheet resistivity, sheet carrier concentration and mobility of the surface layer. Sheet carrier concentrations are obtained from Hall effect measurements using a van der Pauw configuration. Differential resistivity and Hall effect measurements in conjunction with successive layer removal are used to obtain the electrical carrier distributions as a function of the laser fluence. We observe that for good quality crystalline regrowth and full electrical activation, the laser fluence should lie between the melting threshold and damage threshold.

#### 3.5.1 Hall System

The schematic diagram of the double a.c. Hall system [43] is shown in Fig. 3.8. A sample current of about 0.3 mA, at a frequency of 1 kHz and a 200 Gauss magnetic field at 250 Hz were used. The Hall voltage



LP-1176

Figure 3.8. Block diagram of the double ac Hall system.

appears at the heterodyne frequency of 750 Hz. Buffer stages are placed between the mixer and both oscillator stages and also before the current inputs to the sample, thereby achieving significant noise reduction. Three stages of tuned active filters are used to generate the 750 Hz reference. The final two stages are the reference channels of the PAR JB-5 and HR-8 lock-in amplifiers.

### 3.5.2 Sample Preparation

After implantation and laser annealing the samples were subjected to anodic oxidation. An anomalous surface layer, sometimes observed in heavily implanted samples, causes a rough etched surface. This surface layer was removed by anodic oxidation [44] prior to chemical etching. In this process ~ 100 Å of the Si surface was removed, as estimated from measurement of the anodic oxide thickness. This surface treatment was performed on all samples used in electrical measurements after laser annealing.

After implantation, laser annealing, and anodic oxidation stripping, electrical contacts were formed by evaporating Au through a shadow mask and then sintering at 200°C in flowing H<sub>2</sub> for 15 sec. The samples were then defined photolithographically in a van der Pauw geometry. Using a diluted planar chemical etch [45], successive Si layers were removed. To minimize the uncertainty due to possible variation in the etch rate, etched step heights were measured at various points in the profile, using a Dektak stylus. In the case of such high dose B implanted Si, the ratio of Hall mobility to conductivity mobility was taken to be 0.73, appropriate for high concentration p-regions [46]. The van der Pauw geometry and the sample holder are shown in Figure 3.9.

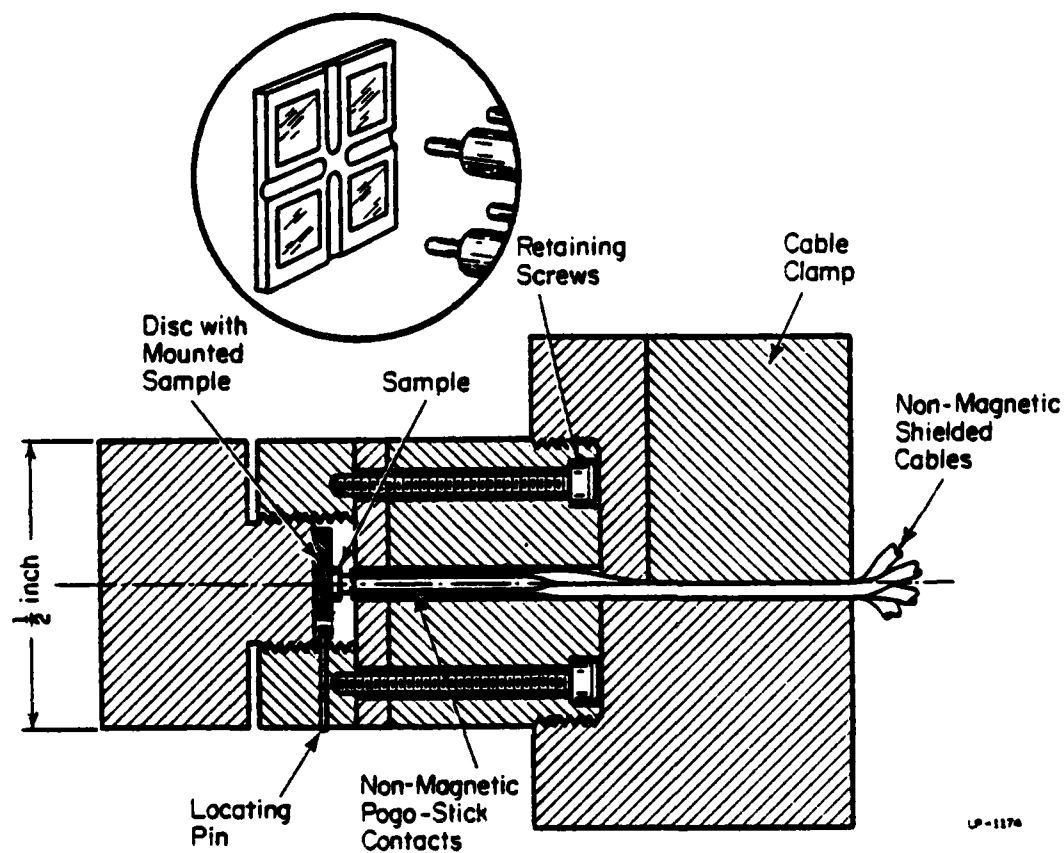


Figure 3.9. Cross sectional view of the sample holder used for double ac van der Pauw measurements. The insert shows the sample configuration and spring loaded contacts in the holder.

### 3.5.3 Data Analysis

The sheet resistivity  $\rho_s$  and sheet Hall coefficient  $R_s$  are given by

$$\rho_s = \frac{\pi}{\ln 2} \frac{V_{ABCD} + V_{BCDA}}{2I} f\left(\frac{V_{ABCD}}{V_{BCDA}}\right) \quad (3.3)$$

and

$$R_s = \frac{\sqrt{2} \Delta V_{BDAC} \text{ (rms)}}{B(\text{rms}) I(\text{rms})} \quad (3.4)$$

Here  $V_{ABCD}$  represents the voltage between contacts A and B with current  $I$  passed between C and D.  $V_{BCDA}$  and  $\Delta V_{BDAC}$  are similarly defined, with  $\Delta V_{BDAC}$  the Hall voltage in a magnetic field,  $B$ . The correction factor  $f(V_{ABCD}/V_{BCDA})$  is Van der Pauw's factor. Let the sheet resistivities before and after stripping a layer of thickness  $d_j$  be denoted by  $\rho_{s_j}$  and  $\rho_{s_{j-1}}$ ; similarly,  $R_{s_j}$  and  $R_{s_{j-1}}$  refer to sheet Hall coefficients. The average mobility  $\mu_j$  of the layer is given by

$$\mu_j = \frac{R_{s_j}}{\rho_{s_j}} + \frac{R_{s_{j-1}}}{\rho_{s_{j-1}}} - \frac{R_{s_{j-1}} - R_{s_j}}{\rho_{s_{j-1}} - \rho_{s_j}} \quad (3.5)$$

and the average carrier concentration is given by

$$n_j = \frac{\frac{1}{\rho_{s_j}} - \frac{1}{\rho_{s_{j-1}}}}{e d_j \mu_j} \quad (3.6)$$

Here, the Hall coefficient factor, which is the ratio of the Hall mobility to conductivity mobility, is assumed to be 0.73.

### 3.5.4 Experimental Results

In Figure 3.10 the acceptor concentration and mobility profiles are compared with the boron atomic profile for the sample irradiated with a laser fluence of  $1.0 \text{ J/cm}^2$ . We observe that for a laser fluence of  $1.0 \text{ J/cm}^2$ , there is nearly full electrical activation to a depth of  $\sim 1300 \text{ \AA}$ , the boundary of the original amorphous-crystalline interface (I). Beyond  $\sim 1300 \text{ \AA}$ , there is no electrical activation. We also note from Figure 3.7 that the peak fluorine concentration occurs near  $\sim 1200 \text{ \AA}$ . For a pulse of  $1.0 \text{ J/cm}^2$ , the temperature rises to a value below the melting point of amorphous silicon, producing annealing by solid phase epitaxial regrowth. The termination of the active acceptor profile at I is consistent with results of furnace annealing [31].

Figure 3.11 - 3.14 shows plots of the acceptors and mobility profiles for laser fluences of 2.0, 2.5, 3.5 and  $4.0 \text{ J/cm}^2$  respectively. All these fluences induce melting as observed by time resolved reflectivity measurements.

Figure 3.12 shows a plot of the electrical carrier profile for a laser fluence of  $2.5 \text{ J/cm}^2$ , which produces melting and redistribution of the boron profile. In this case there is less than 100% electrical activation to a depth of  $\sim 2000 \text{ \AA}$ . The peak electrical carrier concentration is a factor of 1.5 less than the peak atomic profile. We note from Figure 3.7 that the peak fluorine concentration at  $\sim 1200 \text{ \AA}$  is slightly higher than that of the as-implanted sample and there is a second smaller fluorine peak at  $\sim 2250 \text{ \AA}$ , beyond which we find no electrical activation. Thus, there appears to be a relation between electrical activation and the fluorine distribution.

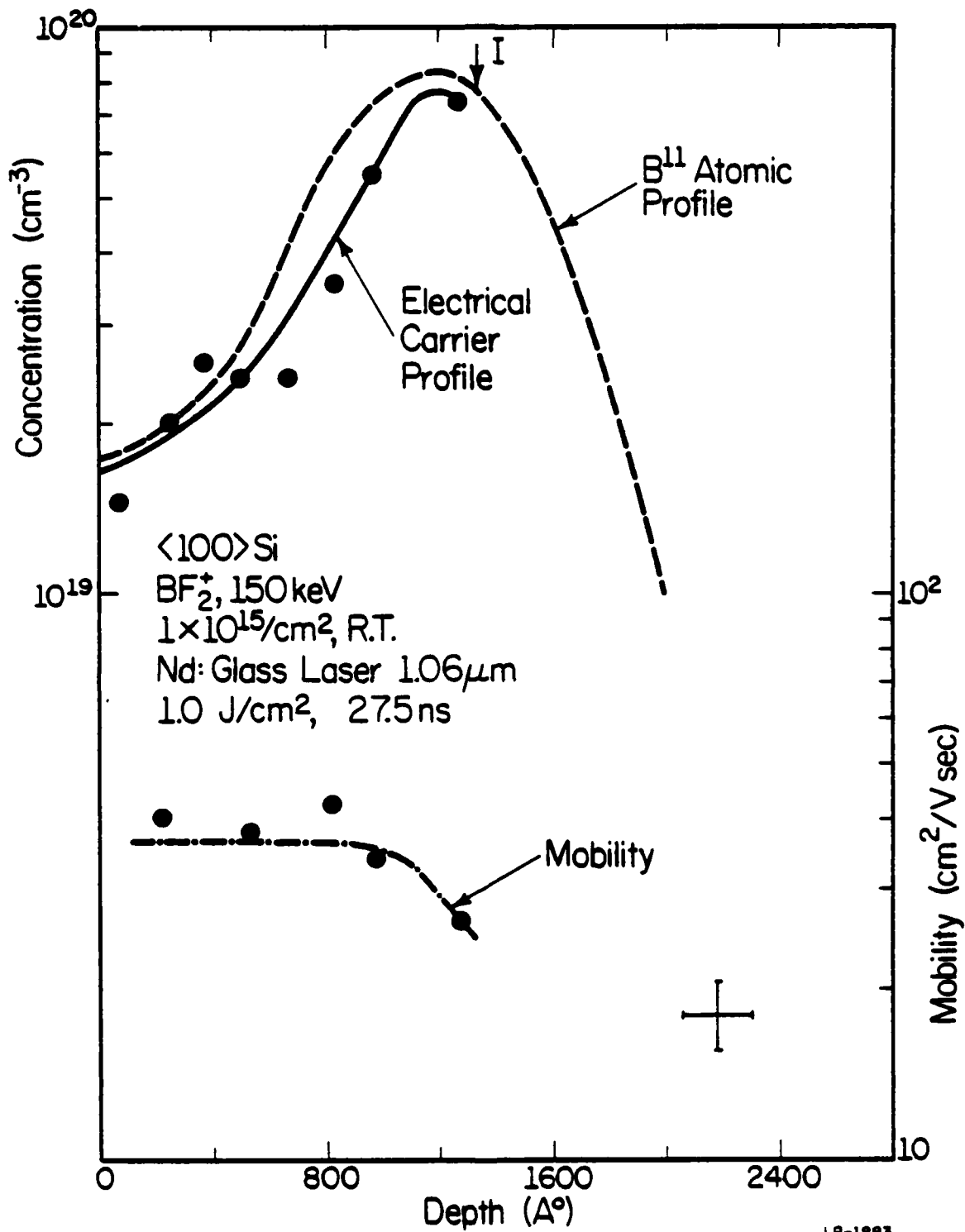


Figure 3.10 Net acceptor concentration and mobility profiles for the sample irradiated with  $1.0 \text{ J}/\text{cm}^2$ . The boron atomic profile is also shown for comparison.

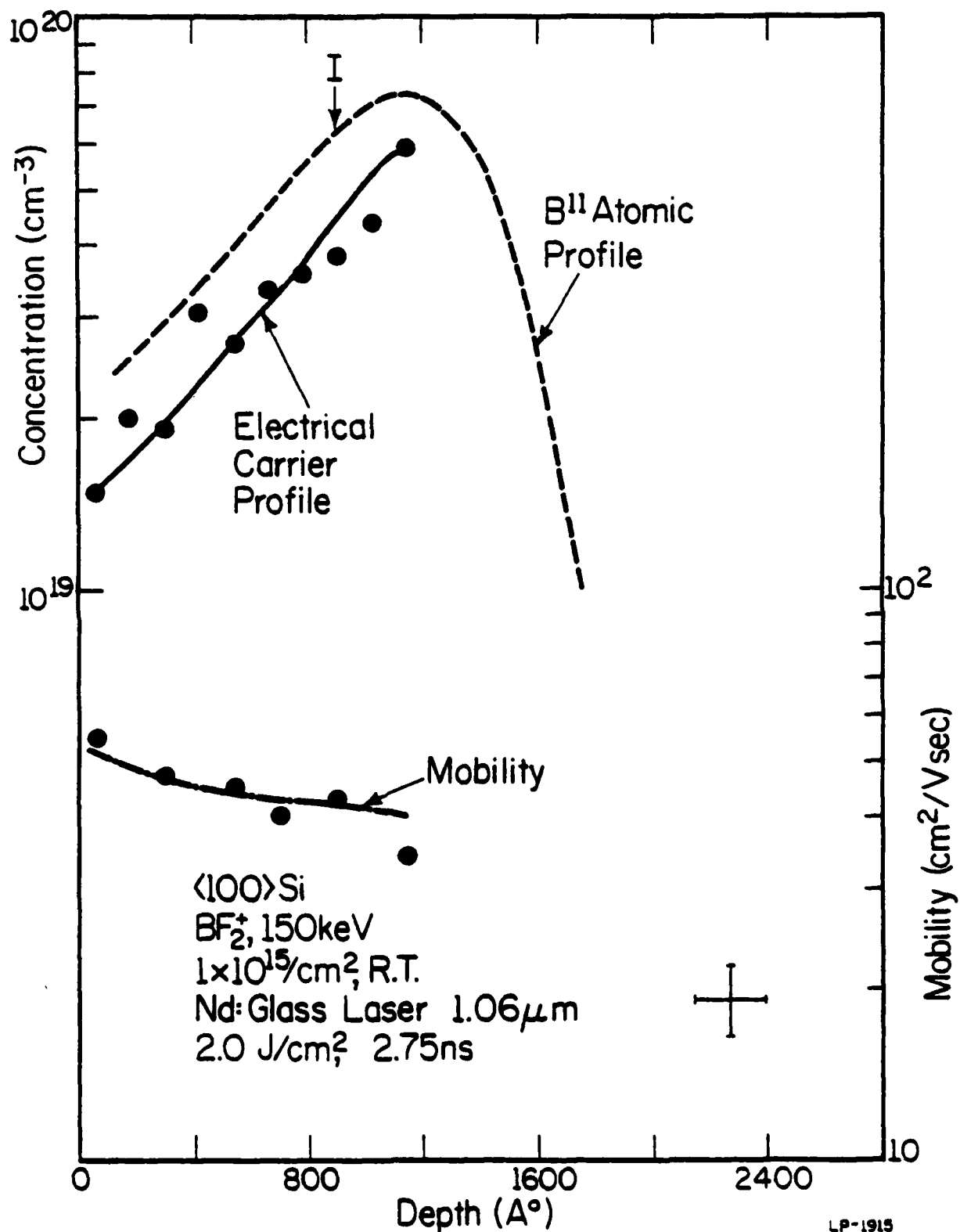


Figure 3.11. Net acceptor concentration and mobility profiles for the sample irradiated with  $2.0 \text{ J}/\text{cm}^2$ .

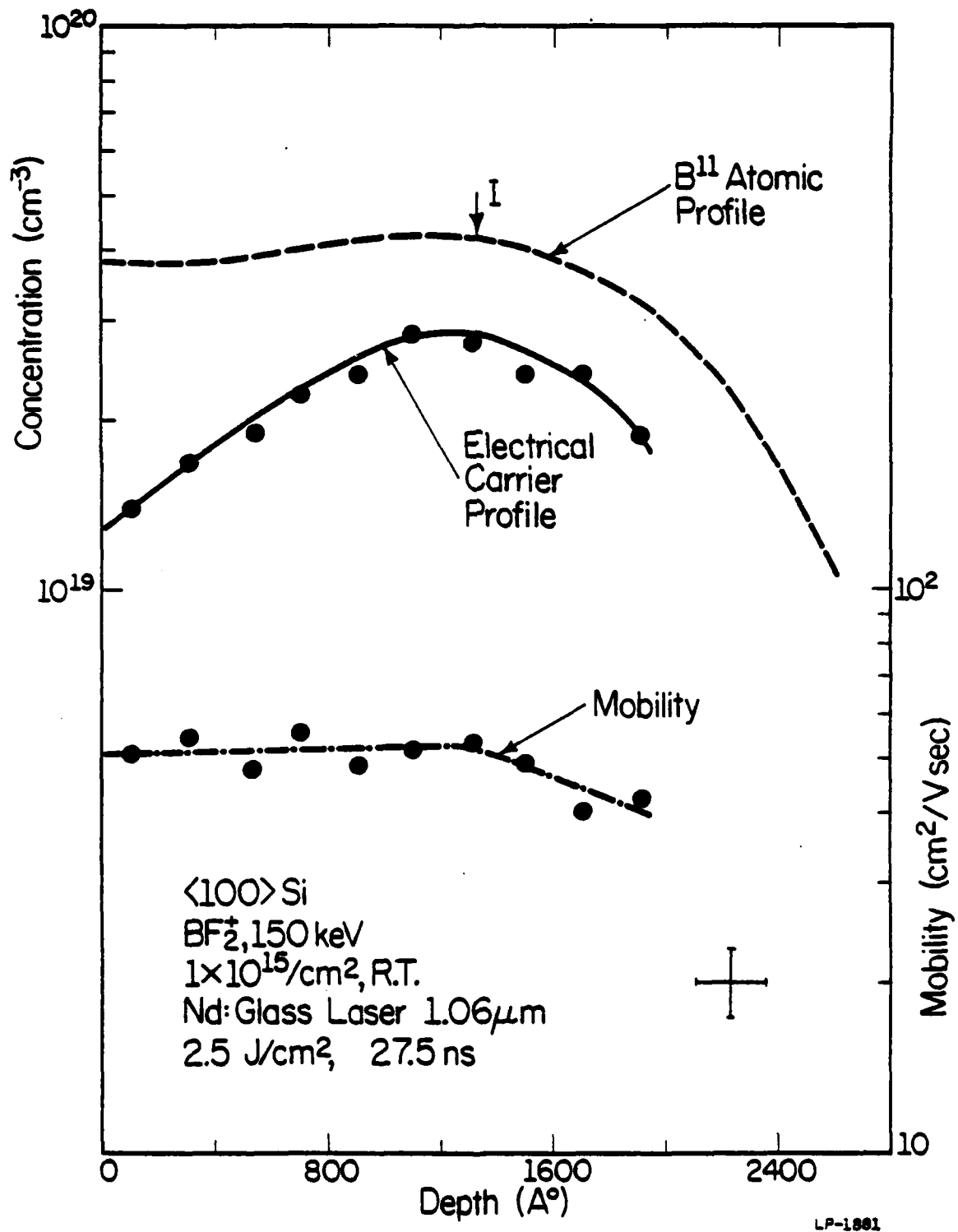


Figure 3.12. Net acceptor concentration and mobility profiles for the sample irradiated with 2.5 J/cm<sup>2</sup>. The boron atomic profile is also shown for comparison.

Figure 3.13 and 3.14 shows similar plots of acceptors and mobility profiles for laser fluence of 3.5 and 4.0 J/cm<sup>2</sup> respectively. For this rather high laser fluence there is nearly 100% electrical activation to a depth of ~ 2250 and ~ 2500 Å respectively. Also there is no electrical activation beyond ~ 2400 and ~ 2750 Å for 3.5 and 4.0 J/cm<sup>2</sup> laser fluences. From Figure 3.7 we find there is a second fluorine peak at ~ 2500 Å (for 3.5 J/cm<sup>2</sup>) and ~ 2700 Å (for 4.0 J/cm<sup>2</sup>).

For full electrical activation with pulsed laser annealing, it is absolutely necessary to choose the laser fluence such that the melt front penetrates deeper than the defect tail beyond the amorphous-to-crystalline interface [47].

The fluorine concentration after the laser pulse seems to be influenced by the distribution of the residual defect concentration. The above discussion of fluorine migration and electrical activation profiles clearly suggests the influence of residual defects. The preferential migration of fluorine to a defect-rich region is similar to the ion-damage gettering discussed by Seidel et al.[48] and by Tsai et al. [32]. For all the laser fluences the damaged region responsible for fluorine gettering also gives rise to the electrically inactive tail of the boron distribution. For the 2.5, 3.5 and 4.0 J/cm<sup>2</sup> fluences, a defect-rich region occurs well below the original amorphous-to-crystalline interface [49].

### 3.6 Electron Channeling Pattern using a Scanning Electron Microscope

To investigate the material properties of the amorphized layer before and after the laser pulse, we employed the technique of electron channeling using a scanning electron microscope. For the as-implanted material there was no electron channeling pattern, confirming the presence

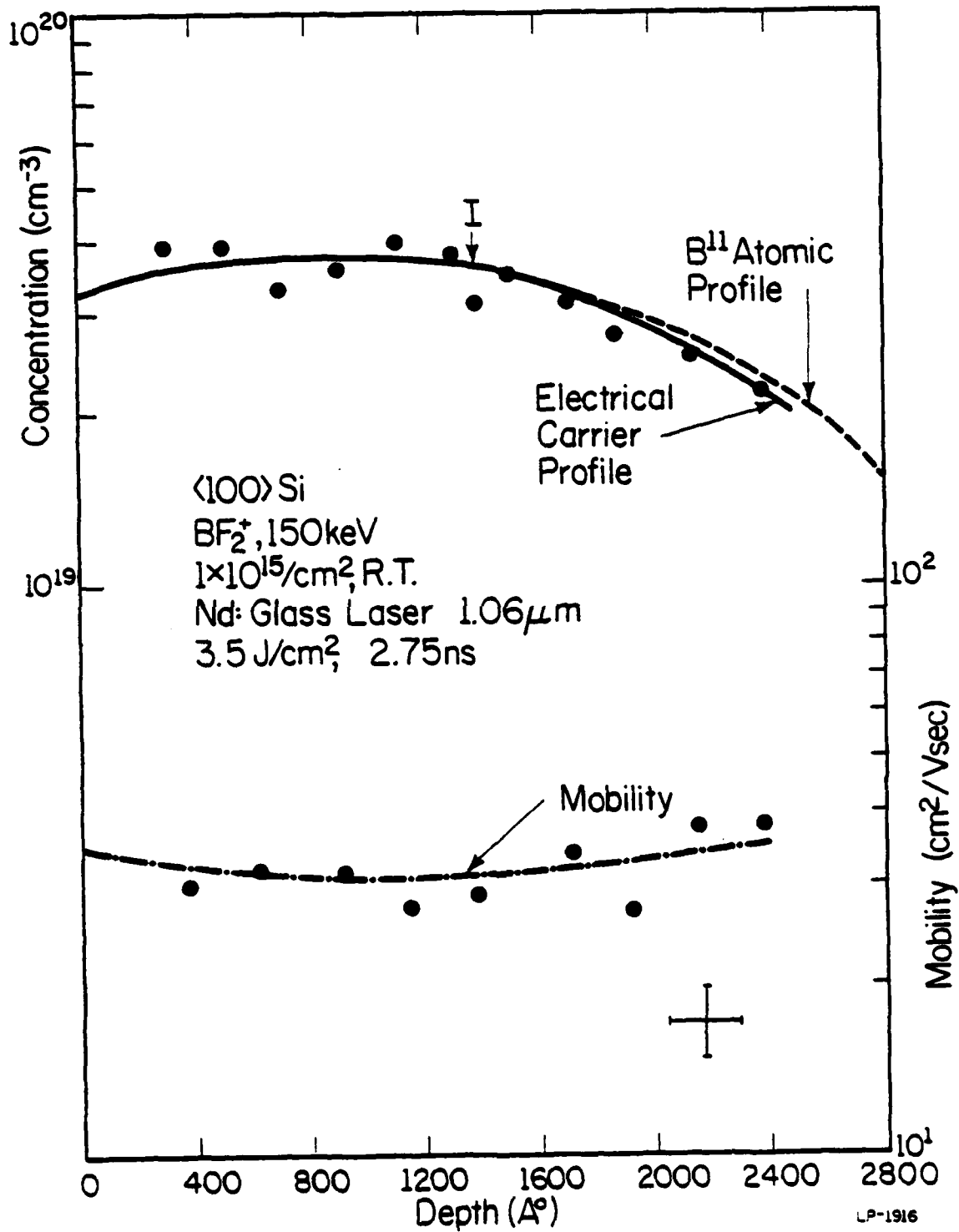


Figure 3.3. Net acceptor concentration and mobility profiles for the sample irradiated with  $3.5 \text{ J}/\text{cm}^2$ . The boron atomic profile is also shown for comparison.

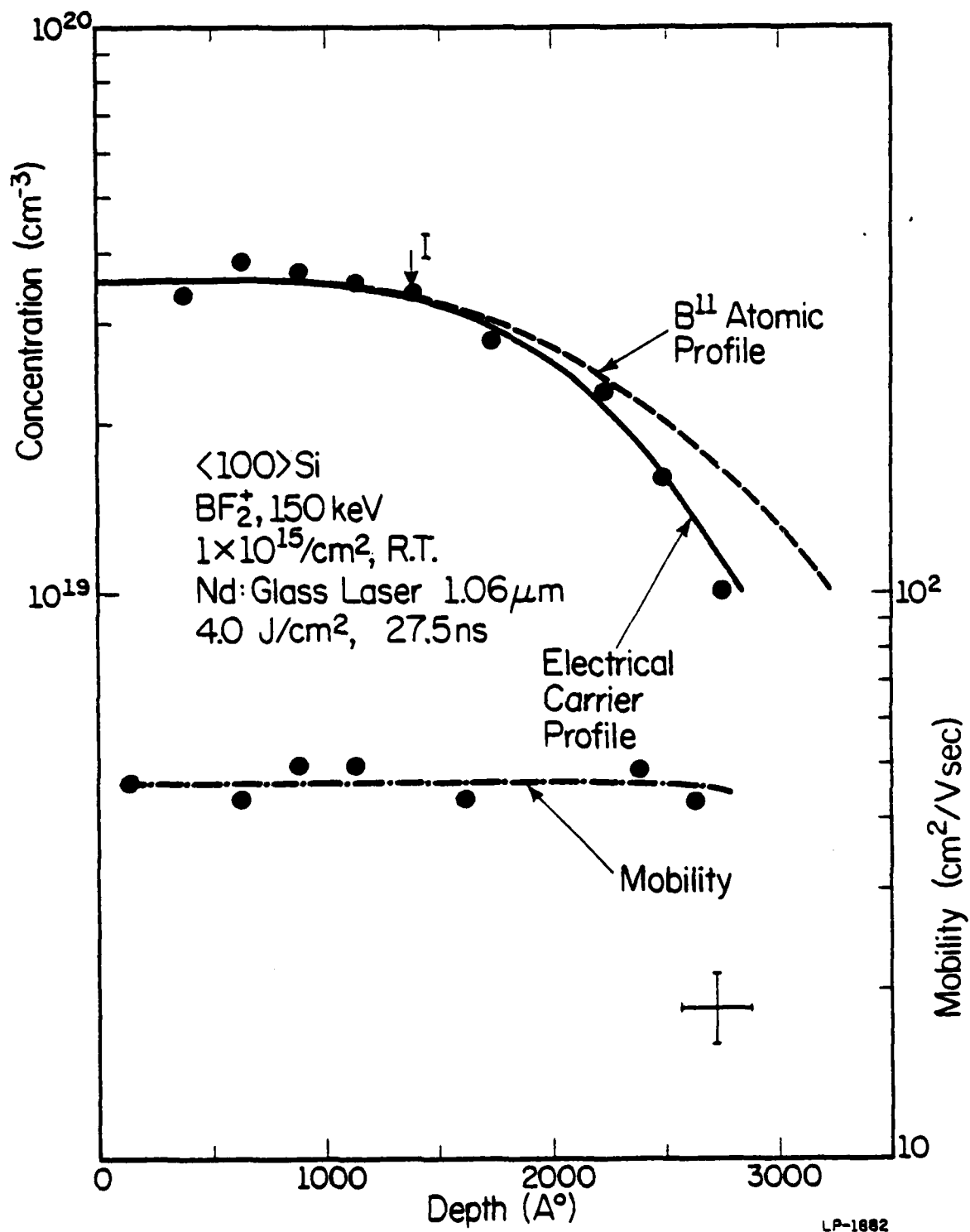


Figure 3.14. Net acceptor concentration and mobility profiles for the sample irradiated with  $4.0 \text{ J}/\text{cm}^2$ . The boron atomic profile is also shown for comparison.

of an amorphous layer. The sample that was irradiated with a  $4.0 \text{ J/cm}^2$  laser fluence clearly showed an electron channeling pattern due to the crystalline regrowth of the amorphous layer. The regrown layer has a  $\langle 100 \rangle$  orientation, as expected for recrystallization on the  $\langle 100 \rangle$  substrate. A typical picture of the channeling pattern is shown in Fig. 3.15.

The channeling pattern shown in Fig. 3.15 is as sharp as that obtained from an unimplanted sample from the same wafer. This supports the fact that a fluence of  $4.0 \text{ J/cm}^2$  is sufficient for the melt-front to move through the original amorphous-crystalline interface, as predicted from the calculations.

Nd: Glass Laser  
4.0 J/cm<sup>2</sup>

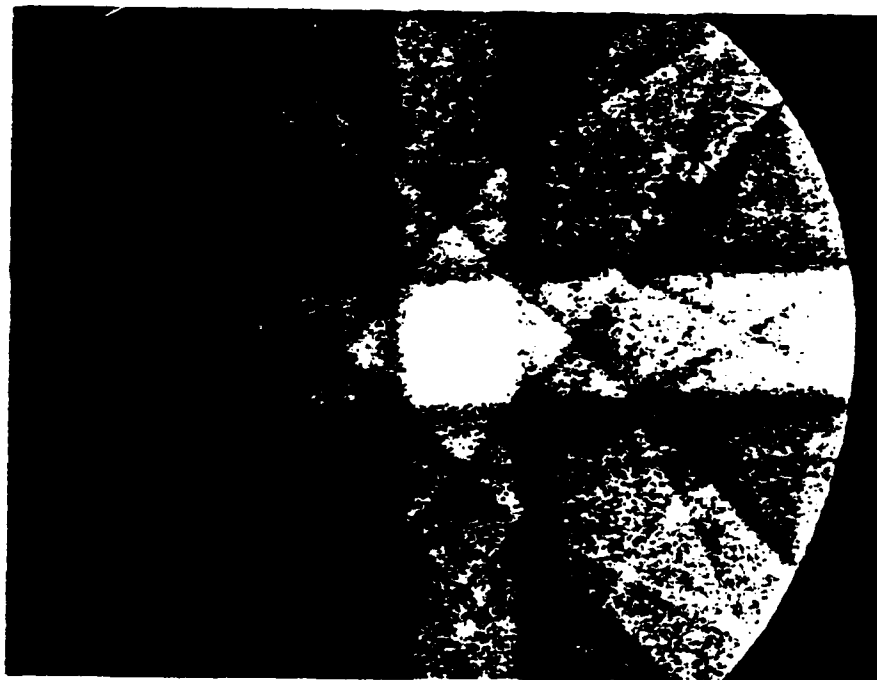


Figure 3.15. Electron channeling pattern of the  $\text{BF}_2^+$  implanted amorphous Si  $\langle 100 \rangle$  after irradiation with a laser pulse of 4.0 J/cm<sup>2</sup>.

#### 4. DYNAMICS OF PULSED CO<sub>2</sub> LASER ANNEALING OF SILICON

Pulsed lasers have been successfully applied for annealing of radiation damage associated with ion-implantation in Si during device fabrication. Experimentally, work has been mainly confined to laser wavelengths in the visible and near-infrared using a frequency doubled YAG laser at  $\lambda = 0.53 \mu\text{m}$  [3] and a Nd:glass laser at  $\lambda = 1.06 \mu\text{m}$  [36]. In all these lasers the spot-size of the laser beam on the Si sample was typically a few mm in diameter. Hence, to anneal a large area it was necessary to use successive overlapping pulses, leading to nonuniform crystalline quality in the overlap regions. Pulsed CO<sub>2</sub> lasers have the distinct advantage of having considerably larger spot-size, and are therefore very promising for laser annealing of large Si wafers commonly used in industrial production. At 10.6  $\mu\text{m}$ , the absorption coefficient of amorphous silicon is much smaller than that of crystalline silicon having large donor concentration. Hence, for annealing with a CO<sub>2</sub> laser it is advantageous to implant the sample with a moderately high ion dose without driving the sample amorphous.

We present a detailed calculation using the method of finite differences to study the dynamics of pulsed CO<sub>2</sub> laser annealing of ion-implanted Si. The calculations are based on a thermal melting model, taking into account the temperature dependences of all pertinent material parameters, including the absorption coefficient. We investigate the "thermal runaway" behaviour and calculate the threshold power density to cause thermal runaway and surface melting of Si during CO<sub>2</sub> laser annealing.

We present results from a quantum mechanical calculation of the temperature variation of the free carrier absorption coefficient for n-type Si at 10.6  $\mu\text{m}$ . We report on the application of the temperature dependent

absorption coefficient to investigate the rise in surface temperature leading to thermal runaway during CO<sub>2</sub> laser annealing of Si. We have calculated the power density required to initiate the thermal runaway situation. Our results are in good agreement with those observed experimentally [50,51]. In calculating the absorption coefficient we have adjusted the deformation potentials such that the calculated values agree with the available experimentally obtained values [52,53] at 300° K. It is well known that at 10.6 μm the absorption mechanism in Si is primarily due to free carriers, with a small contribution due to multiphonon excitations. The variation of absorption coefficient with temperature provides insight into the mechanism by which laser power couples into the material. We find that the absorption coefficient increases rapidly with temperature, resulting in a "thermal runaway" situation for large power densities. This can lead to melting of the implanted layer as observed experimentally, and subsequent liquid-phase epitaxial regrowth [51] during pulsed CO<sub>2</sub> laser annealing.

We calculate the contributions from the acoustic deformation potential scattering ( $\alpha_{ac}$ ), optical deformation potential scattering ( $\alpha_{op}$ ), and ionized impurity scattering ( $\alpha_{io}$ ), and add them together to give the total free carrier absorption coefficient ( $\alpha$ ) as a function of temperature from 300° K to 1685° K (the melting point of Si):

$$\alpha = \alpha_{ac} + \alpha_{op} + \alpha_{io} \quad (4.1)$$

We have taken into consideration the contribution from both the electrons and holes for completeness, although the holes contribute little for n-type Si. The data presented are for the case of thermal equilibrium with the electron temperature equal to the lattice temperature ( $T_e = T$ ).

The free carrier absorption coefficient for the acoustic deformation potential scattering is given by

$$\alpha_{ac} = \frac{\mu_0 c^2 \cdot 2^{3/2} n e^2 \epsilon_{ac}^2 (m^* k_B T)^{1/2}}{\sqrt{\kappa} 3\pi \hbar^3 c_\ell \omega} \left[ \frac{T}{T_e} \right]^{1/2} \sinh \left[ \frac{\hbar \omega}{2k_B T_e} \right] K_2 \left[ \frac{\hbar \omega}{2k_B T_e} \right] \quad (4.2)$$

where  $\mu_0 c = 377$  ohm,  $n$  is the free carrier concentration,  $\epsilon_{ac}$  is the acoustic deformation potential constant,  $\kappa$  is the dielectric constant of the material,  $c_\ell$  is the longitudinal elastic constant,  $m^*$  is the effective mass of electrons (holes), and  $K_2$  is the modified Bessel function of the second order. The contribution of electrons and holes toward  $\alpha_{ac}$  is calculated by using the parameters given in reference [54]. A factor of 2 is taken into account in equation (4.2) to consider both the phonon absorption and emission processes.

We note that in the case of thermal equilibrium ( $T_e = T$ ) and high temperature, Eq. 4.2 reduces to that obtained by using the classical Drude model. The dependence of  $\alpha_{ac}$  on the carrier temperature  $T_e$  in this approximation is given by

$$\alpha_{ac} \propto T_e^{-1/2} \quad (4.3)$$

In the quantum limit  $\hbar \omega \gg 2k_B T_e$  the absorption becomes independent of  $T_e$ . The absorption is stronger in the quantum limit than it is in the classical limit, but the dependence on  $\lambda$  is less strong ( $\propto \lambda^{5/2}$ , compared with  $\lambda^2$  in the classical limit).

The total concentration of electrons is obtained by assuming that all the donors are ionized at  $300^{\circ}$  K, each contributing one electron. The number of holes is obtained from the charge neutrality condition and the relation  $np = n_i^2$ . The total free carrier concentration is given by the sum of electron and hole concentrations.

The equations for the optical deformation potential scattering and ionized impurity scattering are also obtained from Ref. 55. For thermal carriers and at long wavelengths,  $\alpha_{op} \propto \lambda^2$ . This is the same as for acoustic scattering. For  $\alpha_{op}$  we note that for small  $T_e$ ,  $\alpha_{op}$  is nearly independent of  $T_e$ , whereas for large  $T_e$   $\alpha_{op}$  is proportional to  $T_e^{1/2}$ . For the ionized impurity scattering,  $\alpha_{io}$  is proportional to the product  $nN_d$ , where  $N_d$  is the impurity (donor) concentration. Since for an uncompensated semiconductor in the extrinsic range  $N_d = n$ , we observe an increase of  $\alpha_{io}$  with  $n^2$  rather than with  $n$  as in the previous cases where phonons were involved.

Figure 4.1 shows the total free carrier absorption coefficient in n-Si as a function of carrier concentration for various wavelengths at  $300^{\circ}$  K. The deformation potentials are adjusted so that the calculated values agree with the experimentally observed values [52,53]. We note that for a particular value of the free carrier concentration the absorption coefficient is larger for longer wavelengths. Also, for a particular wavelength, the absorption coefficient increases linearly with concentration.

Figure 4.2 shows the variation of the total free carrier absorption coefficient with temperature for various concentrations of ionized donor impurities. We note that for the lower values of the donor concentrations ( $N_d = 10^{16}/\text{cm}^3$ ,  $10^{17}/\text{cm}^3$ ) and  $T < 700^{\circ}$  K, the total number of free carriers is basically given by the number of electrons contributed by the ionized

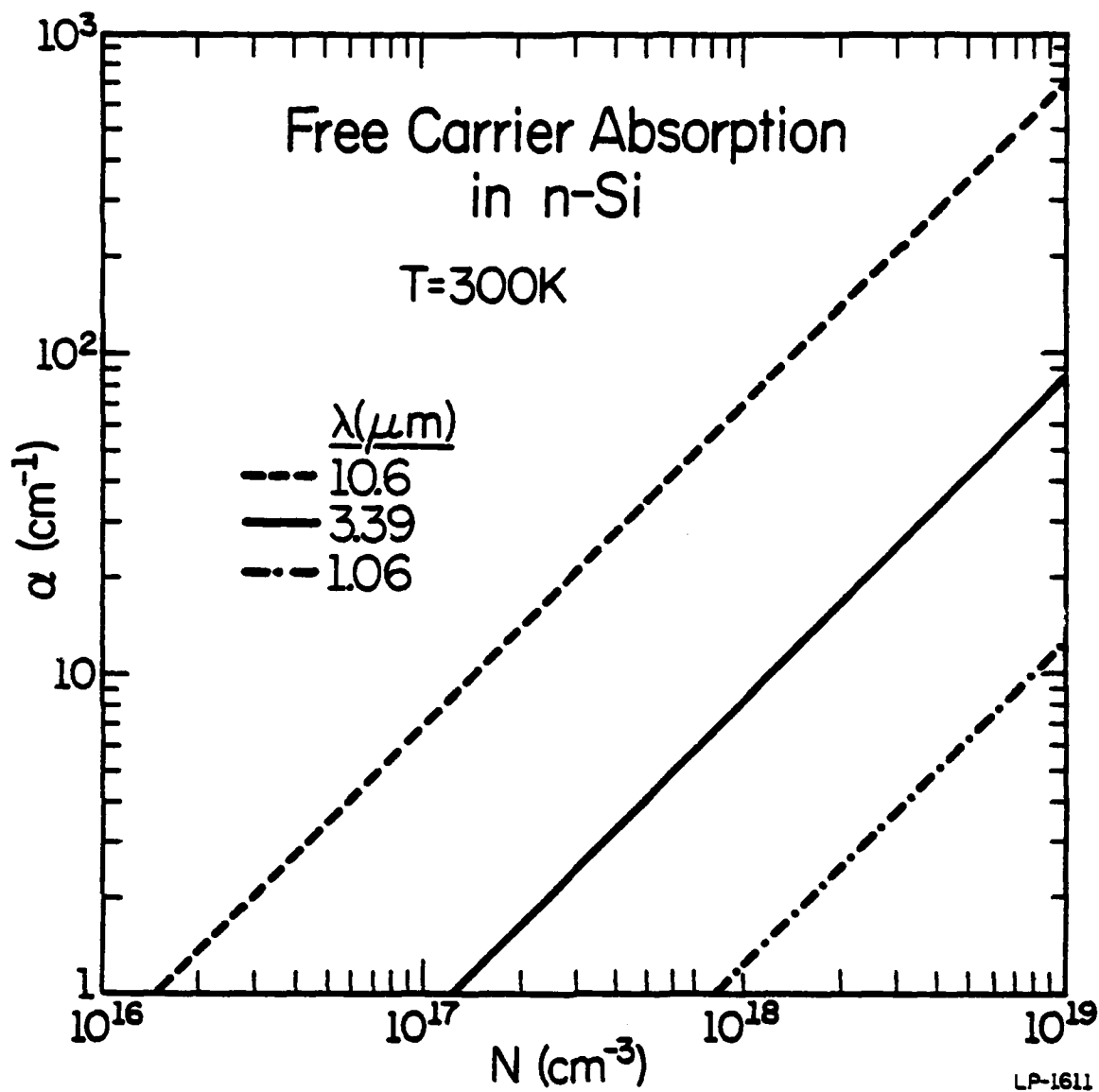


Figure 4.1. Variation of the free carrier absorption coefficient with carrier concentration for n-Si at 300°K for different wavelengths.

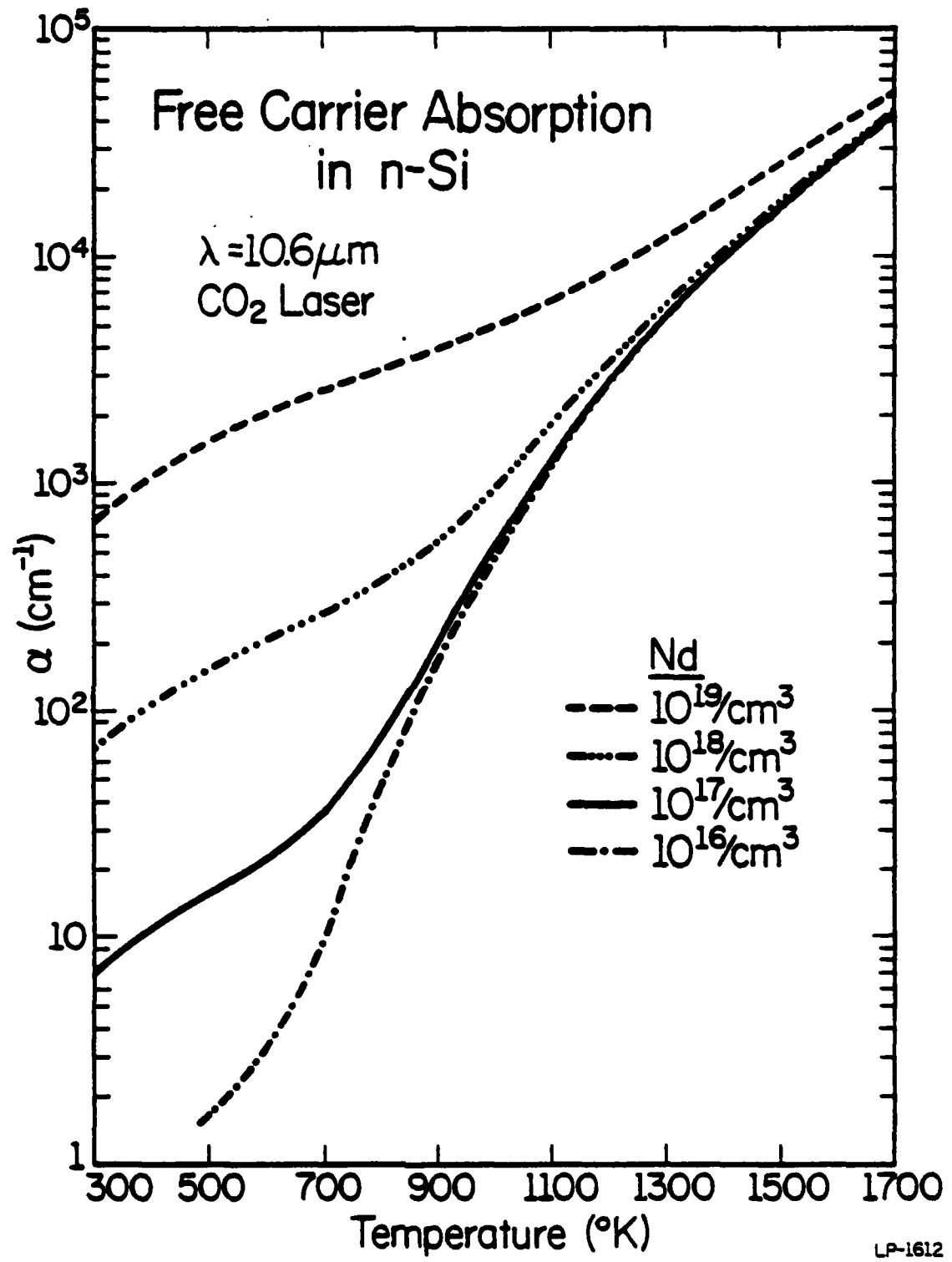


Figure 4.2. Variation of the free carrier absorption coefficient at 10.6  $\mu\text{m}$  with temperature for n-Si with different donor impurity concentrations.

donors. At temperatures  $T > 700^\circ \text{K}$ , however, the number of free carriers contributed by the intrinsic carrier concentration becomes comparable to that contributed by the ionized donors, and the absorption coefficient rises rather sharply. For  $N_d = 10^{18}/\text{cm}^3$ , the value of the absorption coefficient rises from a value of  $70.0/\text{cm}$  at  $300^\circ \text{K}$  to a value of  $4.0 \times 10^4/\text{cm}$  at  $1685^\circ \text{K}$ . This rapid increase of absorption coefficient explains the thermal runaway observed during  $\text{CO}_2$  laser annealing of ion-implanted silicon [51]. We also note that at  $1685^\circ \text{K}$  the values of  $\alpha$  for  $N_d = 10^{16}$ ,  $10^{17}$ , and  $10^{18}/\text{cm}^3$  approach the same value of  $4.0 \times 10^4/\text{cm}$ , whereas that for  $N_d = 10^{19}/\text{cm}^3$  approaches a value of  $5.0 \times 10^4/\text{cm}$ . So, for efficient coupling of the laser energy to the material, it is advisable to start with Si which has been implanted with an ionized donor impurity of moderately high dose (resulting in a donor concentration of  $10^{18} - 10^{19}/\text{cm}^3$ ). Alternatively, the sample can be maintained at a reasonably high temperature before the laser energy is incident so that enough free carriers are generated to ensure a large absorption coefficient. Thus, Fig. 4.2 can be used in choosing appropriate experimental conditions for pulsed or cw  $\text{CO}_2$  laser annealing of ion-implanted Si. The results of Fig. 4.2 for  $10.6 \mu\text{m}$  can be fitted by an empirical power law. For  $N_d = 10^{18}/\text{cm}^3$ :

$$\alpha = 1.016 \times 10^{-2} T^{1.55}, \quad 300^\circ \text{K} < T < 600^\circ \text{K}$$

$$\alpha = 4.593 \times 10^{-5} T^{2.38}, \quad 600^\circ \text{K} < T < 800^\circ \text{K}$$

$$\alpha = 5.559 \times 10^{-19} T^{7.083}, \quad 900^\circ \text{K} < T < 1685^\circ \text{K}$$

A similar fit can be obtained for the other donor concentrations.

These approximations can be used in choosing the laser and the material parameters and substrate temperature for successful laser annealing.

We now apply our calculations of the temperature dependent absorption coefficient to investigate the thermal runaway problem during pulsed CO<sub>2</sub> laser annealing of Si.

The temperature in the solid is obtained from the solution of the one-dimensional heat flow equation

$$C(T)\rho \frac{\partial T}{\partial t} = \frac{\partial}{\partial x} \left[ \kappa(T) \frac{\partial T}{\partial x} \right] + E(1-R)ae^{-\alpha x} \quad (4.4)$$

where  $\kappa$  is the thermal conductivity,  $C$  is the specific heat  $\rho$  is the density,  $E$  is the laser power density, and  $R$  is the reflection coefficient.

For simplicity, we assume  $\kappa$  and  $C$  to be temperature independent.

Equation (4) reduces to

$$\frac{\partial T}{\partial t} = D \frac{\partial^2 T}{\partial x^2} + \frac{E(1-R)ae^{-\alpha x}}{C\rho} \quad (4.5)$$

where  $D = \kappa/C\rho$ .

We note that when  $\alpha$  is small, i.e., the absorption length is large ( $\alpha^{-1} \gg \sqrt{Dt}$ ), we can neglect the heat conduction and determine the temperature at any point from the absorbed energy. This is no longer valid when the temperature increases to the point that

$$\alpha^{-1}(T_c) = \sqrt{Dt}.$$

In the low temperature approximation, equation (4.5) simplifies to

$$\frac{\partial T}{\partial t} = \frac{E(1-R)}{C\rho} ae^{-\alpha x} \quad (4.6)$$

We now apply equation (4.6) to find the temperature at the surface for various laser power densities  $E$ .

The temperature variation of the absorption coefficient can be expressed by

$$\alpha = ae^{T/T_1} \quad (4.7)$$

For  $N_d = 10^{19}/\text{cm}^3$  and  $\lambda = 10.6 \mu\text{m}$ , we find  $a = 317.48/\text{cm}$  and  $T_1 = 346^\circ \text{K}$ .

The solution to (6) for the surface temperature is then given by

$$T(0,t) = T_0 + T_1 \ln \left[ 1 - \frac{\alpha(T_0)E(1-R)t}{\rho CT_1} \right]^{-1} \quad (4.8)$$

where  $T_0$  is the initial temperature. For Si we have assumed  $\kappa = 1.40 \text{ W/cmK}$ ,  $C = 0.74 \text{ J/cmK}$ , and  $\rho = 2.33 \text{ g/cm}^3$  in the solid phase. The value of  $R$  at  $10.6 \mu\text{m}$  is 0.30.

To investigate the thermal runaway behavior we have plotted in Figure 4.3. The surface temperature as a function of time for various laser power densities. The pulse length was chosen to be 25 nanoseconds. We observe from Figure 4.3 that for low laser power densities the temperature rise is not fast enough to initiate thermal runaway during the 25 ns laser pulse. However, for power densities  $\geq 75 \text{ MW/cm}^2$  we observe a dramatic increase of the surface temperature, leading to thermal runaway. This minimum power density  $E \approx 75 \text{ MW/cm}^2$  is in good agreement with observed experimental values [50,51]. We note that as the absorption coefficient becomes large with increased temperature we cannot apply equation (4.8). In Figure 4.3, the surface temperatures for laser power densities  $\geq 50 \text{ MW/cm}^2$  have been calculated up to a value  $T_C$  such that  $\alpha^{-1}(T_C) \approx \sqrt{Dt}$ . For temperatures higher than  $T_C$  equation (4.8) is no longer valid since then we have the condition  $\alpha^{-1}(T > T_C) < \sqrt{Dt}$ .  $T_C$  is given by the expression  $T_C = T_1 \ln \left[ \frac{1}{a\sqrt{Dt}} \right]$ . For lower values of  $N_d$ , the absorptor coefficient is smaller and the minimum power density to induce thermal runaway becomes larger.

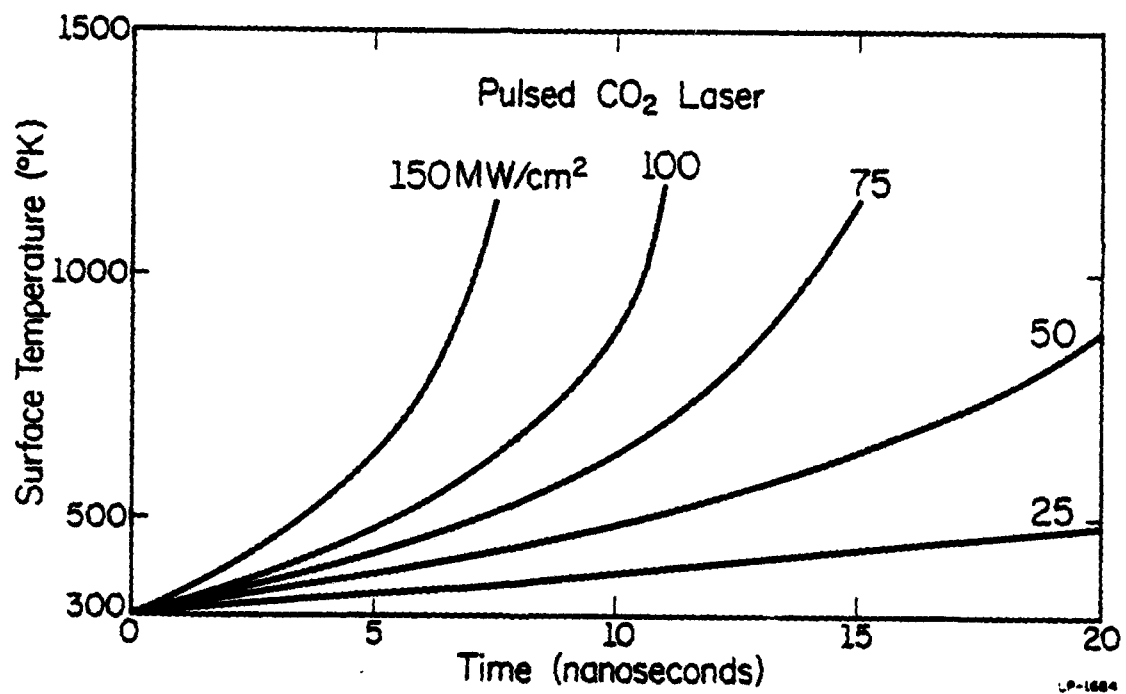


Figure 4.3. Surface temperature of n-Si with  $N_d = 10^{19}/\text{cm}^3$  during CO<sub>2</sub> laser pulses (25 nsecs) for various laser power densities.

The above simplified model enables us to calculate only the surface temperature to investigate the "thermal runaway" phenomenon. We now apply the melting model taking into account the temperature variation of all the material parameters to investigate the phenomenon of melting and regrowth with a pulsed CO<sub>2</sub> laser.

The one-dimensional heat flow is described by the equation

$$C(T) \rho \frac{\partial T}{\partial t} = \frac{\partial}{\partial x} \left[ \kappa(T) \frac{\partial T}{\partial x} \right] + S(x,t) \quad (4.9)$$

where  $\kappa$  is the thermal conductivity,  $C$  is the specific heat capacity, and  $\rho$  is the density of the material. The source term  $S$  is governed by the mechanism of laser-solid interaction and the time shape of the laser pulse. The laser pulse is assumed to be Gaussian, and so the time-dependent part of the source term is given by

$$S(t) = \frac{1}{\pi^{1/2} \Gamma} \exp \left[ - \left( \frac{t-t'}{\Gamma} \right)^2 \right] \quad (4.10)$$

where  $\Gamma$  is the parameter which determines the full width at half maximum (FWHM) and  $t'$  is the time when the pulse reaches its maximum value.

The spatial part of the source term is given by

$$S(x) = E \alpha(x) (1-R) \exp \left( - \int_0^{\infty} \alpha(x') dx' \right) \quad (4.11)$$

where  $E$  is the laser fluence in J/cm<sup>2</sup>,  $R$  is the reflectivity, and  $\alpha$  is the temperature-dependent absorption coefficient. During melting and freezing the latent heat  $L$  has been accounted for. We do this by holding the temperature constant until enough heat is absorbed or rejected to account for the latent heat.

To solve equation (4.9) numerically by the method of finite differences we divide the sample into equal sections of length  $\Delta x$ . The time step is  $\Delta t$ . The intervals  $\Delta x$  and  $\Delta t$  are chosen to satisfy the von Neumann stability criterion given by

$$\Delta t < \frac{C_p}{2\kappa} (\Delta x)^2$$

specifically, we choose  $\Delta x = 250 \text{ \AA}$  and  $\Delta t = 2 \text{ ps}$  for our calculations.

The temperature dependence of the free carrier absorption coefficient at  $10.6 \text{ }\mu\text{m}$  for n-Si has been calculated [39] by taking into account acoustical deformation potential scattering, optical deformation potential scattering, and ionized impurity scattering. For an ionized donor impurity concentration of  $N_d = 10^{19}/\text{cm}^3$  the temperature variation of the absorption coefficient is given by

$$\alpha(T) = \alpha e^{T/T_1}$$

where  $\alpha = 3.17 \times 10^2/\text{cm}$  and  $T_1 = 346 \text{ K}$ . The absorption coefficient increases with a rise in the concentration of carriers. Also, the absorption coefficient increases nonlinearly with temperature, leading to "thermal runaway" and thermal melting.

A typical temperature vs. time profile for n-Si with  $N_d = 10^{19}/\text{cm}^3$  irradiated with a pulsed  $\text{CO}_2$  laser of 25 ns FWHM and laser fluence of  $1.875 \text{ J/cm}^2$  is shown in Figure 4.4. The shape of the laser pulse is shown in the bottom left-hand corner. The notation  $T_m$  denotes the melting point of silicon, which is 1685 K. We note that for temperatures  $T < 700 \text{ K}$ , when  $\alpha$  is small and the absorption length is large, the temperature rises rather slowly and is mainly determined by the absorbed energy with negligible thermal conduction. However, as  $\alpha$  increases rapidly with temperature, the slope of the temperature rise becomes steeper, heat is more absorbed in the near surface

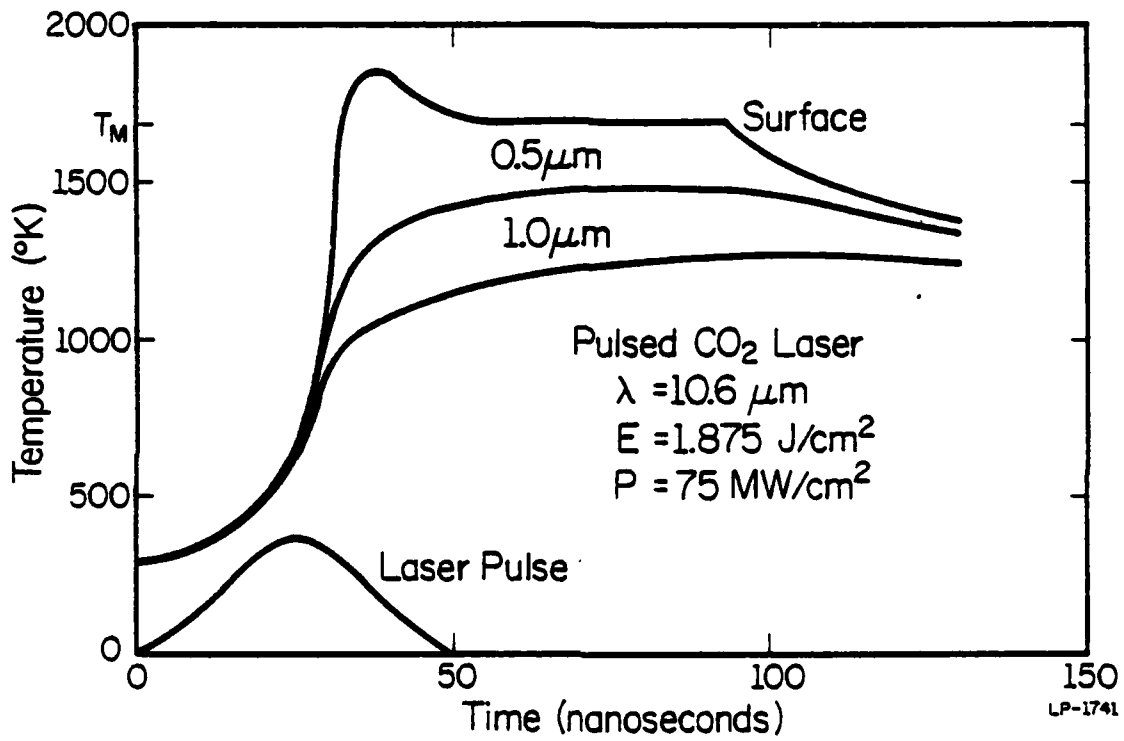


Figure 4.4. Results of the calculation showing the temperature vs. time profiles at the surface and at depths of 0.5  $\mu\text{m}$  and 1.0  $\mu\text{m}$  for n-Si with  $N_d = 10^{19}/\text{cm}^3$  and a CO<sub>2</sub> pulse (25 ns FWHM) of 1.875 J/cm<sup>2</sup>.

region of the solid, and thermal conduction becomes important. We note that a laser fluence of  $1.875 \text{ J/cm}^2$  is sufficient to initiate "thermal runaway", eventually leading to surface melting. We also note that the peak of the laser pulse occurs at 25 ns, whereas the maximum surface temperature (1930 K) occurs at 37.5 ns. From Figure 4.4 we find that the front surface remains molten for a period of time  $\tau_m = 60 \text{ ns}$ . This time  $\tau_m$  can be verified experimentally using similar time-resolved reflectivity measurements as discussed for a Nd:glass laser [36]. In Figure 4.4 we have also plotted the temperature profile at  $0.5 \mu\text{m}$  at  $1.0 \mu\text{m}$ . We note that deep into the material the maximum temperature is smaller and the temperature peak occurs at a later time, as expected. For  $1.875 \text{ J/cm}^2$ , we find from our data that the melt front needs a maximum distance of  $0.15 \mu\text{m}$ .

In Figure 4.5 we have plotted the temperature profile in the sample at different times for a laser fluence of  $2.5 \text{ J/cm}^2$ . The maximum surface temperature of 2430 K occurs at 35 ns. We note that in the beginning of the pulse the slope of the curve is rather flat, indicating that for small  $\alpha$  (large absorption length), the sample is heated rather uniformly. However, as the temperature increases, the absorption length decreases and the surface is heated rapidly. The strongest variation of temperature with distance occurs at 30 ns, when the surface temperature reaches its maximum value. With further increase in time, the curve becomes flatter again as heat is transmitted away by thermal conduction.

Figure 4.6 shows a plot of the maximum surface temperature and the maximum depth of melting ( $x_M$ ) for various laser fluences. We note that a laser fluence of  $1.25 \text{ J/cm}^2$  causes "thermal runaway" but the surface temperature rises to a maximum value of only 920 K. To have surface melting, a

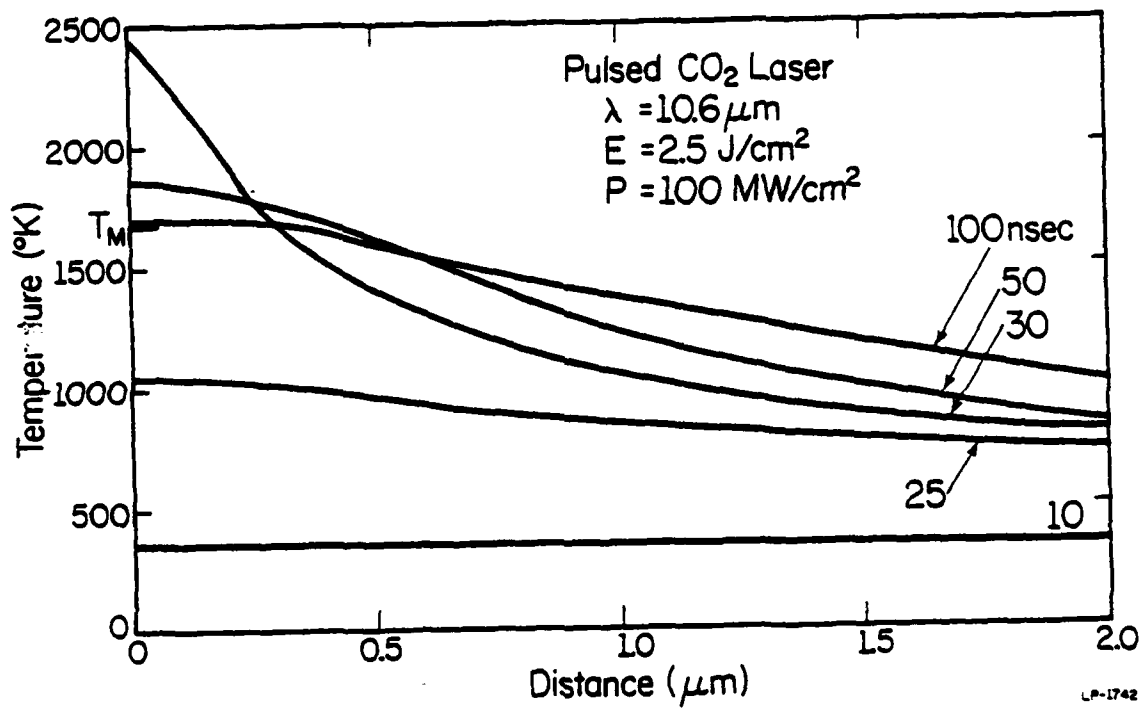


Figure 4.5. Calculated temperature vs. distance profiles at various times for a laser fluence of  $2.5 \text{ J/cm}^2$  (25 ns FWHM).

minimum laser fluence  $E_{\min}$  of  $\sim 1.52 \text{ J/cm}^2$  is necessary. As the laser fluence is increased beyond  $E_{\min}$ , the maximum surface temperature increases and the depth of melting also increases. Typically, to melt a layer of  $0.4 \mu\text{m}$  requires a laser fluence of  $2.45 \text{ J/cm}^2$ , as can be seen from Figure 4.6.

Figure 4.7 shows the variation of the duration of surface melting ( $\tau_m$ ) as the laser fluence is increased from the threshold value for melting ( $1.52 \text{ J/cm}^2$ ). We find that for fluence  $1.52 < E < 1.65 \text{ J/cm}^2$  the value of  $\tau_m$  increases rather sharply. Beyond  $1.65 \text{ J/cm}^2$  the slope of the curve decreases. However, for laser fluences  $> 1.85 \text{ J/cm}^2$ , the slope of the curve again increases. This variation of  $\tau_m$  is comparable to the variation of the maximum surface temperature for  $1.52 < E < 2.5 \text{ J/cm}^2$  as shown in Fig. 4.6. Once the laser fluence increased beyond the melting threshold, we would expect a marked variation of  $\tau_m$  with  $E$  as shown for  $1.52 < E < 1.65 \text{ J/cm}^2$ . The change in  $\tau_m$  for the three different regions of the curve is primarily governed by the magnitude of the laser fluence relative to the threshold value ( $E_{\min}$ ) for melting.

Our calculations [56] give a physical picture of the dynamics of pulsed  $\text{CO}_2$  laser annealing. The model provides values of laser fluences or power densities required to melt a particular thickness for a laser pulse of  $25 \text{ ns}$  (FWHM). The graphs presented here are for  $N_d = 10^{19}/\text{cm}^3$ ; one can calculate similarly the melting threshold  $E_{\min}$  for other concentrations of ionized donor impurities. We note that since  $\alpha$  decreases, the value of  $E_{\min}$  consequently increases.

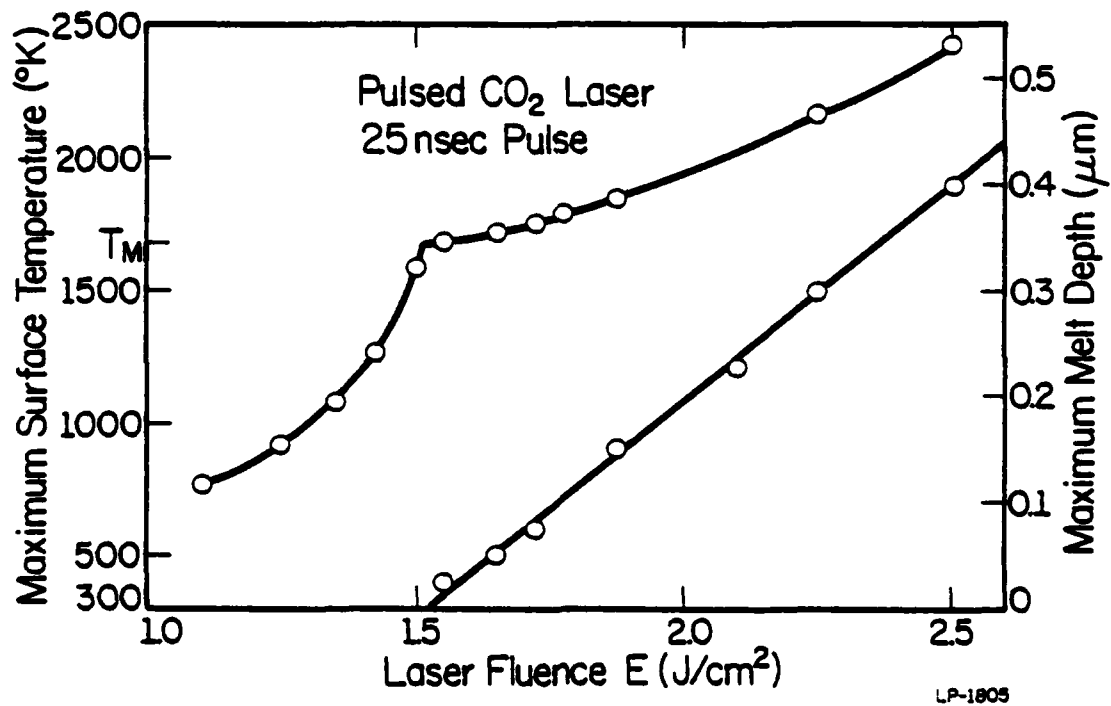


Figure 4.6. Maximum surface temperature and maximum melt depth as a function of the laser fluence (25 ns FWHM).

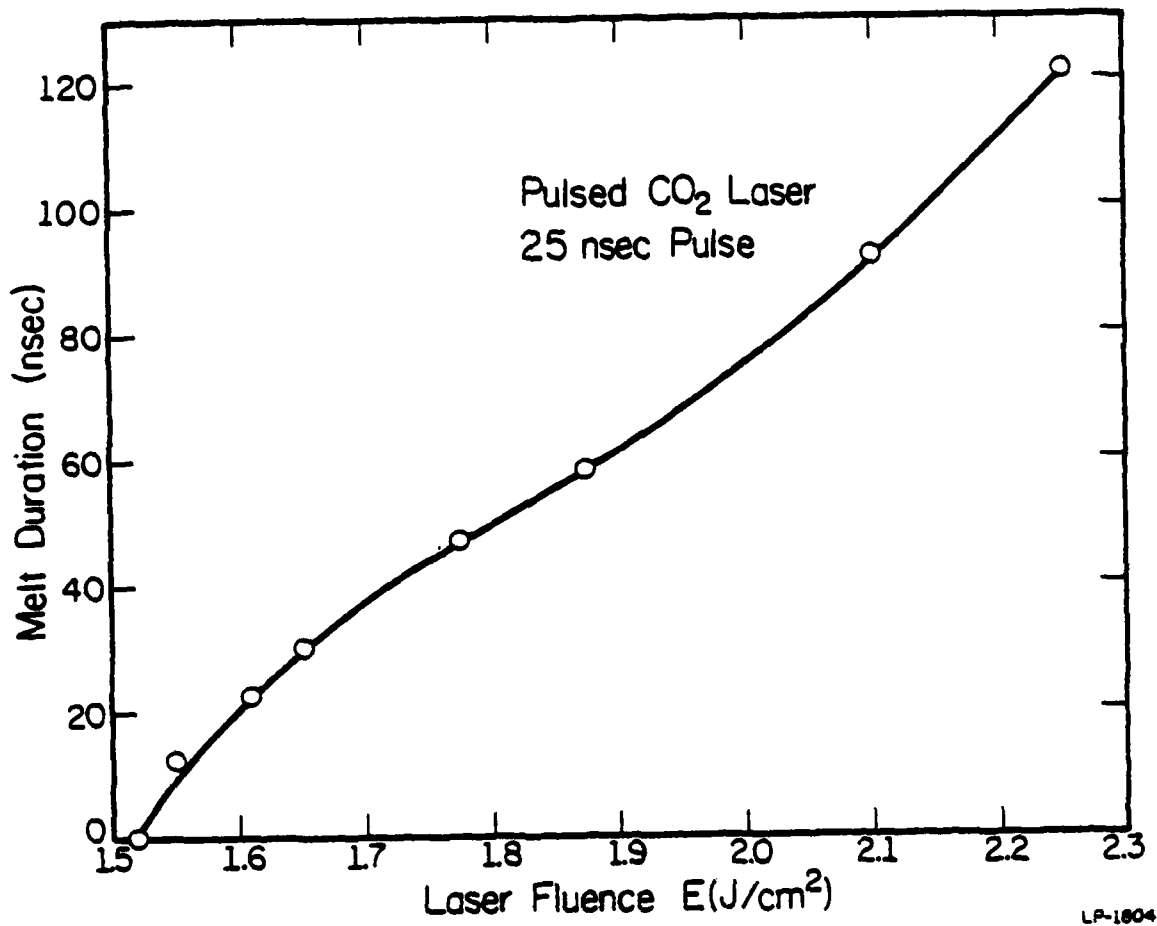


Figure 4.7. Duration of surface melting vs. laser fluence (25 ns FWHM).

## REFERENCES

1. I. B. Khaibullin, E. I. Shtyrov, M. M. Zaripov, R. M. Bayazitov, and M. F. Galjautdinov, *Radiat. Eff.* 36, 225 (1978) and references therein.
2. A. E. Bell, *RCA Review*, 40, 295 (1979).
3. C. M. Surko, A. L. Simons, D. H. Auston, J. A. Golovchenko, and R. E. Slusher, *Appl. Phys. Lett.* 34, 635 (1979).
4. J. C. Wang, R. F. Wood, and P. P. Pronko, *Appl. Phys. Lett.* 33, 455 (1978).
5. L. Jastrzebski, A. E. Bell, and C. P. Wu, *Appl. Phys. Lett.* 35, 608 (1979).
6. B. L. Crowder, R. S. Title, M. H. Brodsky, and G. D. Petit, *Appl. Phys. Lett.* 16, 205 (1970).
7. J. A. Van Vechten, R. Tsu, F. W. Saris and D. Hoonhout, *Physics Letters*, 74A, 417 (1979).
8. H. W. Lo and A. Campaan, *Appl. Phys. Lett.* 44, 1604 (1980).
9. M. I. Nathan, R. T. Hodgson and E. J. Yoffa, *Appl. Phys. Lett.* 36, 512 (1980).
10. J. C. Schultz and R. J. Collins, *Appl. Phys. Lett.* 34, 85 (1979).
11. A. J. Glassbrenner and G. A. Slack, *Physical Review* 134, A1058 (1964).
12. Selected Values of Thermodynamic Properties of the Elements, edited by R. T. Hultgren, P. D. Desai, D. T. Hawkins, M. Gleiser, K. K. Kelley, and D. D. Wigwan (American Society for Metals, Metals Park, Ohio, 1973).
13. D. L. Keune, Monsanto Co. (private communication).
14. P. Baeri, S. U. Campisano, G. Foti, and E. Rimini, *J. Appl. Phys.* 50, 788 (1979).
15. H. R. Philipp, *J. Phys. Chem. Solids* 32, 1935 (1971).
16. K. M. Shvarev, B. A. Baum, and P. V. Gold, *Sov. Phys. Solid State* 16, 2111 (1975).
17. J. F. Gibbons, *Proc. IEEE*, 56, 295 (1968).
18. J. F. Gibbons, *Proc. IEEE*, 60, 1062 (1972).
19. J. W. Mayer, L. Erickson, and J. A. Davies, Ion Implantation in Semiconductors, Academic Press, New York (1970).

20. P. L. Degen, Phys. Status Solidi A, 16, 9 (1973).
21. D. H. Lee and J. W. Mayer, Proc. IEEE, 62, 1241 (1974).
22. J. Lindhard and A. Winther, Mat. Fys. Medd. Dan. Vid. Selsk., 34, 1 (1964).
23. O. B. Firsov, J. Exper. Theoret. Phys., 36, 1517 (1959).
24. S. Lindhard, M. Scharff, and H. Schiott, Mat. Fys. Medd. Dan. Vid. Selsk., 33, 1(1963).
25. J. F. Gibbons, W. S. Johnson, and S. W. Mylroie, Projected Range Statistics, 2nd edition, Halstead Press, Stroudsburg, Penn. (1975).
26. B. L. Crowder, R. S. Title, M. H. Brodsky, and G. D. Pettit, Appl. Phys. Lett., 16, 205 (1970).
27. H. J. Stein, F. L. Vook, D. K. Brice, J. A. Borders, and S. T. Picraux, Ion Implantation, Gordon and Breach, London (1971).
28. F. L. Vook, Radiation Damage and Defects in Semiconductors, Institute of Physics, London (1972).
29. F. F. Morehead, Jr. and B. L. Crowder, Rad. Effects, 6, 27 (1970).
30. J. F. Gibbons, Proc. IEEE, 60, 1062 (1972).
31. M. Y. Tsai and B. G. Streetman, J. Appl. Phys., 50, 183 (1979).
32. M. Y. Tsai, D. S. Day, B. G. Streetman, P. Williams, and C. A. Evans, Jr., J. Appl. Phys., 50, 188 (1978).
33. H. S. Carslaw and J. C. Jaeger, Conduction of Heat in Solids, Second edition, Clarendon Press (1976).
34. A. J. Zaremba, G. T. Marcyk, and B. G. Streetman, IEEE Trans. Elec. Devices, ED-24, 163(1977).
35. D. H. Auston, J. A. Golovchenko, A. L. Simons, and C. M. Surko, Appl. Phys. Lett., 34, 777 (1979).
36. Anjan Bhattacharyya, B. G. Streetman and K. Hess, J. Appl. Phys., 52, 3611 (1981).
37. Anjan Bhattacharyya, L. A. Reinisch and B. G. Streetman, Proceedings of the Fourth International Conference on Silicon Materials Science and Technology sponsored by the Electrochemical Society, (1981).
38. G. L. Miller, D. V. Lang, and L. C. Kimerling, Ann. Rev. Mater. Sci., 7, 377 (1971).

39. Anjan Bhattacharyya and B. G. Streetman, *Solid State Communications*, 36, 671 (1980).
40. D. J. Godfrey, *J. Electrochem. Soc.*, 127, 606 (1980).
41. C. A. Evans, Jr., *Thin Solid Films*, 19, 11 (1973).
42. C. A. Evans, Jr., *Anal. Chem.*, 47, 855 (1975).
43. W. V. McLevige, P. K. Chatterjee, and B. G. Streetman, *J. Phys. Ed. Sci. Instrum.*, 10, 335 (1977).
44. J. A. Davies, G. C. Ball, F. Brown and B. Domeij, *Can. J. Phys.*, 42, 1070 (1964).
45. W. R. Runyan, *Semiconductors Measurements and Instrumentation*, McGraw-Hill, New York (1975).
46. K. B. Wolfstrin, *J. Phys. Chem. Solids*, 16, 279 (1960).
47. Anjan Bhattacharyya, V. Iyer, B. G. Streetman, J. E. Baker and Peter Williams, *Proc. of the 31st Electronic Components Conference sponsored by IEEE* (1981).
48. T. E. Seidel, R. L. Meek, and A. G. Cullis, *J. Appl. Phys.*, 46, 600 (1975).
49. K. L. Wang, Y. S. Lin, and C. Burman, *Appl. Phys. Lett.*, 35, 263 (1979).
50. M. Miyao, K. Ohiju and T. Tokuyama, *Appl. Phys. Lett.*, 35, 227 (1979).
51. G. K. Celler, *AIP Conference Proceeding*, 50, 381 (1979).
52. P. A. Schumann, Jr., W. A. Keenan, and A. H. Tong, *J. Electrochem. Soc.*, 118, 145 (1971).
53. D. K. Schroder, *IEEE Trans. of Electron Devices*, ED-25, 254 (1978).
54. C. Jacoboni, *Solid State Electronics*, 20, 77 (1977).
55. K. Seeger, *Semiconductor Physics*, Springer-Verlag, New York (1973).
56. Anjan Bhattacharyya and B. G. Streetman, *J. Phys. D. Appl. Phys.*, 14, L67 (1981).

## APPENDIX A

COMPUTER PROGRAM FOR CALCULATION OF THE DYNAMICS OF SURFACE  
MELTING DURING PULSED LASER ANNEALING OF AN INFINITE ION-  
IMPLANTED AMORPHIZED SEMICONDUCTOR

This program is titled MELT.FOR. This program is very versatile. It can be used for calculation of the temperature rise and the motion of the melt front during pulsed laser annealing of a semiconductor.

For a particular semiconductor, e.g., Si, Ge, GaAs, one has to supply data for the material parameters. The coupling of the laser and the semiconductor is primarily governed by the absorption coefficient. The laser pulse width is characterized by GAMMA and the fluence is given by energy density in  $\text{J}/\text{cm}^2$ .

This program can be appropriately modified to take into account the substrate effects. This situation arises when one considers an implanted amorphized layer of a few thousand angstroms thickness on a crystalline substrate.



```

WRITE (5,540)
540  FORMAT ('OGAMMA ?')
READ (5,140) GAMMA
140  FORMAT (E10.2)
C
WRITE (5,550)
550  FORMAT ('ODX ?')
READ (5,150) DX
150  FORMAT (E10.2)
C
WRITE (5,560)
560  FORMAT ('ODT ?')
READ (5,160) DT
160  FORMAT (E10.2)
C
WRITE (3,600) RHOS,RHOL,ALPHAS,ALPHAL,REFS,REFL,
2  ENERGY,GAMMA,DX,DT
500  FORMAT(1H1,'RHOS=',F11.3/1HO,'RHOL=',F11.3/
2  1HO,'ALPHAS=',E10.2/1HO,'ALPHAL=',E10.2/
3  'OREFS=',F10.2/'OREFL=',F10.2/1HO,'ENERGY=',
4  F10.2/1HO,'GAMMA=',E10.2/1HO,'DX=',E10.2/
5  1HO,'DT=',E10.2)
C
C  CALCULATE THERMAL CONDUCTIVITIES AND SPECIFIC HEATS
C
KL=0.322
CL=0.915
L=4220
C
DO 50 I=300,2000
IF(I.GT.600) GO TO 1
P1(I)=1386.35*I**(-1.21)
P2(I)=0.19*I**0.24
GO TO 50
1  IF(I.GT.900) GO TO 2
P1(I)=3770.63*I**(-1.36)
P2(I)=0.19*I**0.24
GO TO 50
2  IF(I.GT.1200) GO TO 3
P1(I)=1031.0*I**(-1.13)
P2(I)=0.41*I**0.12
GO TO 50
3  P1(I)=15.49*I**(-0.53)
P2(I)=0.41*I**0.12
50  CONTINUE
C
DO 51 I=300,1999

```

```

AKS(I)=P1(I+1)-P1(I)
ACS(I)=P2(I+1)-P2(I)
BKS(I)=P1(I)-AKS(I)*I
BCS(I)=P2(I)-ACS(I)*I
51 CONTINUE
C
C   INITIALIZATION
C
DO 10 I=0,200
TSOLD(I)=300.
X(I)=FLOAT(I)*DX
KS(I)=1.395
CS(I)=0.7469
10 CONTINUE
C
NMELT=0
NFRONT=0
M=1
XBOLD=0.0
XBNEW=0.0
C
C   CALCULATE CONSTANTS USED IN THE CALCULATION
C
DX1=DX*2.
DT1=DT/RHOS
PS1=0.564*(1.-EXP(-ALPHAS*DX))/DX*ENERGY*(1.-REFS)/GAMMA
DT2=DT/(RHOL*CL)
DT3=L/DT
PL1=0.564*(1.-EXP(-ALPHAL*DX))/DX*ENERGY*(1.-REFL)/GAMMA
KL1=KL/DX
C
C   START OF THE TIME ITERATION
C
DO 20 MM=50,500,50
11 TIME=FLOAT(M)*DT
TEXP=EXP(-(TIME/GAMMA-1.665)**2)
IF(NMELT.EQ.0) GO TO 70
C
C   CALCULATE NEW XB
C
SLOPES=KS(NBOLD)*(TSOLD(NBOLD)-1635.)/(FLOAT(NBOLD)*DX-XBOLD)
IF(XBOLD.EQ.FLOAT(NBOLD-1)*DX) GO TO 15
SLOPEL=KL*(1635.-TLOLD(NBOLD-1))/(XBOLD-FLOAT(NBOLD-1)*DX)
GO TO 13
15 SLOPEL=KL*(TLOLD(NBOLD-1)-TLOLD(NBOLD-2))/DX
13 XBNEW=XBOLD+(SLOPES-SLOPEL)/DT3
NBOLD=IFIX(XBOLD/DX)+1

```

```

NBNEW=IFIX(XBNEW/DX)+1
IF(NFRONT.EQ.1) GO TO 12
C
C CHECK THE SIGN OF FRONT VELOCITY
C
14 IF(XBNEW.GE.XBOLD) GO TO 12
WRITE(3,645) TIME,XBOLD
545 FORMAT(1H1,' MELT FRONT REACHES MAXIMUM AT ',1PE11.3,
2 ' SEC'/1H0,' XBMAX= ',E11.3)
NFRONT=1
GO TO 12
70 NBOLD=0
NBNEW=0
C
C TEMPERATURE IN THE SOLID
C
C
12 DO 30 N=NBOLD+1,199
B3=EXP(-ALPHAS*(X(N)-.5*DX))*TEXP
IF(N.EQ.1) B3=TEXP
PS=PS1*B3
IF(NMELT.EQ.1) PS=0.0
KLEFT=0.5*(KS(N-1)+KS(N))
KRIGHT=0.5*(KS(N+1)+KS(N))
A=-KLEFT*(TSOLD(N)-TSOLD(N-1))
2 +KRIGHT*(TSOLD(N+1)-TSOLD(N))
TSNEW(N)=TSOLD(N)+DT1/CS(N)*(PS+A/(DX*DX))
30 CONTINUE
TSNEW(200)=300.
C
C IF(NMELT.EQ.0) GO TO 33
C
32 IF(NBNEW.GE.NBOLD+1) GO TO 34
DELTEM=(1635.-TSNEW(NBOLD+1))/(FLOAT(NBOLD+1)-XBNEW/DX)
DO 35 N=NBOLD,NBNEW,-1
35 TSNEW(N)=TSNEW(N+1)+DELTEM
34 CONTINUE
IF((NFRONT.EQ.0).OR.(NBNEW.GE.3)) GO TO 53
C
C SURFACE MELTING ENDS
C
C
35 WRITE(3,640) TIME
640 FORMAT(1H1,' SURFACE MELTING ENDS AT ',1PE11.3,' SEC')
XBNEW=0.0
XBOLD=0.0
NBNEW=0
NMELT=0

```

```

NFRONT=0
DO 61 N=0,NBNEW-1
61  TSNEW(N)=1635.
    GO TO 200
33  IF(TSNEW(1).LT.1000.) GO TO 30
    TSNEW(0)=TSNEW(1)-5.3E10*EXP(-4.3E4/TSNEW(1))*DX/KS(1)
    GO TO 200
80  TSNEW(0)=TSNEW(1)
    GO TO 200
C
C  TEMPERATURE IN THE LIQUID
C
63  DO 60 N=1,NBOLD-2
    B4=EXP(-ALPHAL*(X(N)-.5*DX))*TEXP
    IF(N.EQ.1) B4=TEXP
    PL=PL1*B4
    A1=KL1*(TLOLD(N+1)-2.*TLOLD(N)+TLOLD(N-1))
    TLNEW(N)=TLOLD(N)+DT2*(PL+A1/DX)
50  CONTINUE
    IF(TLNEW(1).LT.2000.) GO TO 31
    TLNEW(0)=TLNEW(1)-5.3E10*EXP(-4.3E4/TLNEW(1))/KL1
    GO TO 32
31  TLNEW(0)=TLNEW(1)
32  IF(NBNEW.LE.(NBOLD-1)) GO TO 64
    DELTL=(TLNEW(NBOLD-2)-1635.)/(XBNEW/DX-FLOAT(NBOLD-2))
    DO 62 N=NBOLD-2,NBNEW-2
62  TLNEW(N+1)=TLNEW(N)-DELT1
64  CONTINUE
C
C  CALCULATE NEW THERMAL CONDUCTIVITY AND SPECIFIC HEAT
C
200 DO 52 N=NBNEW,200
    INDEX=IFIX(TSNEW(N))
    IF(INDEX-300) 700,701,701
700  KS(N)=-5.07E-3*TSNEW(N)+2.347
    CS(N)=4.5227E-4*TSNEW(N)+0.613099
    GO TO 52
701  IF(INDEX-2000) 702,703,703
703  KS(N)=-4.3E-5*TSNEW(N)+0.2469
    CS(N)=9.5453E-5*TSNEW(N)+0.3591
    GO TO 52
702  KS(N)=AKS(INDEX)*TSNEW(N)+BKS(INDEX)
    CS(N)=ACS(INDEX)*TSNEW(N)+BCS(INDEX)
52  CONTINUE
    IF(NMELT.EQ.1) GO TO 207
C
C  CHECK INITIAL MELTING

```

AD-A124 465

LASER ANNEALING OF ION IMPLANTED SILICON(U) ILLINOIS  
UNIV AT URBANA COORDINATED SCIENCE LAB A BHATTACHARYYA  
AUG 81 R-912 N00014-79-C-8424

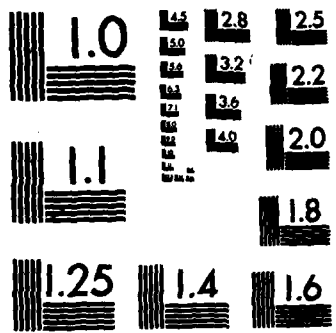
2/2

UNCLASSIFIED

F/G 20/12 NL



END
FILMED
DATE



MICROCOPY RESOLUTION TEST CHART  
NATIONAL BUREAU OF STANDARDS-1963-A

```

C
IF(TSNEW(0).LT.1635.) GO TO 205
DO 71 N=0,200
IF(TSNEW(N)-1635.) 72,71,71
71 CONTINUE
72 XBNEW=DX*FLOAT(N-1)
2 +DX*(TSNEW(N-1)-1635.)/(TSNEW(N-1)-TSNEW(N))
IF(XBNEW.LT.(2.*DX)) GO TO 205
WRITE(3,635) TIME,XBNEW
635 FORMAT(1H1, ' SURFACE MELTED AT ',1PE11.3, ' SEC'
2 /140, ' XBNEW= ',E11.3)
NMELT=1
NBNEW=N
DO 73 N=0,NBNEW-1
73 TLNEW(N)=TSNEW(N)
C
C REPLACE OLD VALUES BY NEW VALUES
C
207 XBOLD=XBNEW
NBOLD=NBNEW
DO 206 N=0,NBNEW-1
206 TLOLD(N)=TLNEW(N)
205 DO 208 N=NBNEW,200
208 TSOLD(N)=TSNEW(N)
C
210 M=M+1
IF(M-MM) 11,40,40
C
C PRINT OUT TIME, XB AND TEMPERATURE
C
40 DO 41 N=NBNEW,200
TP(N)=TSOLD(N)
41 CONTINUE
IF(NBNEW.EQ.0) GO TO 43
DO 44 N=0,NBNEW-1
44 TP(N)=TLOLD(N)
C
43 WRITE(5,610) TIME
610 FORMAT(1H1, ' TIME=',1PE11.3)
WRITE(5,615) XBNEW
615 FORMAT(1H0, ' XB=',1PE11.3)
WRITE(5,620)
620 FORMAT(1H0,4(5X, 'X',3X, 'TEMP',4X))
DO 42 N=0,49
N1=N+50
N2=N1+50
N3=N2+50

```

```
WRITE(5,530) X(N),TP(N),X(N1),TP(N1),X(N2),TP(N2),X(N3),TP(N3)
530  FORMAT(1H ,1PE11.3,7E11.3)
42   CONTINUE
20   CONTINUE
      STOP
      END
```

## VITA

Anjan Bhattacharyya was born on July 2, 1953 in Calcutta, India. He received his Bachelor's degree in Science with Honors in Physics in 1972 from Presidency College, University of Calcutta, India. He then attended Trinity College, University of Cambridge, England where he graduated in 1976 with Honors in Physics and Theoretical Physics and received a B. A. Degree. He was awarded a M. A. degree by the University of Cambridge, England in 1980. Since August 1977 he has been attending the University of Illinois at Urbana-Champaign. He received a Master of Science degree in Physics in January 1979. Mr. Bhattacharyya was awarded a University of Illinois Fellowship in 1978. He is a member of the Institute of Electrical and Electronics Engineers, the American Physical Society, the Electrochemical Society, and the honor society of Phi Kappa Phi.

**END**

**FILMED**

**3-83**

**DTIC**